Improvements in Ultrasound Mediated Drug Delivery using Microbubble Contrast Agents and Application in *Ex-Vivo* Porcine Eyes.

Steven Feingold

A thesis submitted to the faculty of the University of North Carolina at Chapel Hill in partial fulfillment of the requirements for the degree of Master in the Department of Biomedical Engineering

Chapel Hill
2013

Approved by:

Paul A. Dayton, Ph.D.

Gabriela S. Seiler, DVM

Richard L. Goldberg, Ph.D.

Abstract

STEVEN FEINGOLD: Improvements in Ultrasound Mediated Drug Delivery using Microbubble
Contrast Agents and Application in *Ex-Vivo* Porcine Eyes.
(Under the direction of Paul A. Dayton, Ph.D.)

Ultrasound mediated drug delivery is a growing field which shows great promise.
However, the ability to uniformly deliver acoustic energy to large 3D volumes of tissue remains a
challenge for drug delivery. Additionally, uneven drug loading and large size distributions in
microbubble contrast agents (MCAs) reduce the ability to control therapeutic dosing. The aim of
this thesis is to demonstrate improvements in the field through new techniques in producing
acoustically active drug delivery agents and applying ultrasonic parameters to volumetric
regions of interest. The use of a computer controlled motion stage to apply ultrasound to a 3D
volume of tissue is shown, allowing the uniform delivery of destructive pulses and acoustic
radiation force. This technique is demonstrated in a novel application for treating diseases of
the posterior segment of the eye. Injections of MCAs loaded with fluorescent dye into the
suprachoroidal space of *ex-vivo* porcine globes are used to assess the feasibility of ultrasound
mediated drug delivery for treating tissues in the rear of the eye. Also demonstrated is the
production of MCAs with a controlled size and drug loading distribution for oil soluble
compounds, which could enable greater control over therapeutic dosing.

TABLE OF CONTENTS

LIST OF TABLES

Table

LIST OF FIGURES

Figure

Background and introduction

Ultrasound as a therapeutic modality:

Ultrasound has a long history as a diagnostic imaging modality, but is being increasingly pursued as a method for providing therapeutic treatments. Therapeutic effects may be derived directly from the mechanical effects of ultrasound as in HIFU[1] or lithotripsy,[2] or through techniques making use of ultrasound contrast agents. Modern ultrasound contrast agents consist of a core containing high molecular weight gas surrounded by a lipid shell. These micrometer sized liposhperes are known as microbubble contrast agents (MCAs) and are currently widely clinically used in Europe and are available in the US for echocardiography,[3] with clinical trials ongoing for a variety of other diagnostic roles.[4] Clinical ultrasound systems integrate specific imaging strategies which take advantage of the non-linear properties of MCAs to create contrast agent specific images.[5] Due to their size, they are restricted to the vascular space when administered intravenously.[3]

MCAs have several properties which make them ideal for use in therapeutic ultrasound. In the presence of a strong acoustic field, MCAs undergo disruption and destruction along with other phenomena such as jetting[6] and can cause increased inertial cavitation.[7] These events are associated with the creation of small holes in cell membranes (sonoporation)[8], increases in active transport[9] and temporary or permanent weakening of the blood brain barrier.[10] These effects are not currently well understood and are an active area of research[8,10]. Because ultrasound energy can be focused spatially and controlled temporally, these effects can be

highly localized. When MCAs are administered in combination with other drugs, uptake of the drugs can be enhanced locally.[11,12] MCAs can be formulated to carry therapeutic molecules either within[13] or attached to the outside of their encapsulating lipid shell via conjugated nanoparticles or liposomes.[14,15] Therapeutic molecules may include chemotherapeutics,[11] anti-proliferatives[13] and DNA or RNA strands.[16,17] In the presence of strong acoustic pulses, the disruption of MCAs will result in the localized release of the therapeutic payload. By adding ligands to the exterior lipid surfaces, MCAs can target specific markers expressed by diseased or damaged endothelial cells,[18,19] allowing MCAs to concentrate at a site of interest to improve their diagnostic and therapeutic utility.[18-20]

In addition to destruction via strong acoustic pulses, MCAs can be manipulated using acoustic radiation force (ARF). In the presence of an ultrasound field, non-linear oscillators such as MCAs will feel a net force in the direction of sound propagation.[21] By transmitting low intensity-long duration ultrasonic pulses, the net movement is great enough to translate agents out of the central flow of a blood vessel and to the vessel wall.[22] In addition to moving away from the source of the ultrasound MCAs will move laterally towards other MCAs oscillating within the acoustic field,[23] a phenomenon known as secondary radiation force. These two effects both serve to increase the concentration of MCAs where the ultrasonic energy is applied, and have been successfully used *in-vivo* to improve therapeutic effect[14,15] and to improve diagnostic molecular imaging.[24]

While current methods for incorporating drugs into MCAs have proven great promise for many therapeutics, the total drug load is relatively small given the size of MCAs, the physical properties of their shells, and the dilution that occurs when injecting into the blood stream.

Several methods are under investigation for increasing the size and uniformity of the drug payload including liposome attachment,[25] and multilayer design.[26]

Challenges in drug delivery to the eye:

Many applications for therapeutic uses of MCAs have been explored in the literature including, but not limited to, treatment of vessels damaged by stent placement,[13] treatment of Crohn's disease,[16] cancer treatement,[11,17] and providing improving insulin sensitivity.[27] One additional application could be in the treatment of diseases of the posterior portion of the eye. These diseases include age-related macular degeneration, diabetic macular edema and proliferative vitreoretinopathy. Delivering drugs to this region of the eye is difficult for several reasons including the lack external access, the blood-retinal barrier[28] and the choroidal circulation[29]. Current methods for delivering drugs include eye drops and intravitreal and periocular injections. Eye drops remain popular as a non-invasive technique, but often fail to reach the posterior segment of the eye.[28] Periocular injections face physical barriers such as the sclera and choroidal circulation.[29] Intravitreal injections are highly invasive and associated with a number of complications including retinal detachment, cataract formation, elevated intraocular pressure and opacities of the visual axis.[30-32] An alternative location for drug delivery is the suprachoroidal space (SCS), a region which lies between the choroidal and scleral layers. Injections to this space do not penetrate the choroid or the vitreous and are therefore less invasive than intravitreal injections. Previous studies[33,34] have shown that drugs injected into the anterior SCS are capable of reaching the posterior portion of the SCS, and are more effective and have fewer complications[34] than other methods.

MCAs present at least two possible methods of improving drug delivery to the posterior tissues of the eye. One method is to use sonoporation and related effects to weaken the blood-retinal barrier, which has just begun to be investigated.[35] An alternate approach utilizes the ability for ARF to physically move and concentrate MCAs which could allow for intraocular injections to concentrate their payloads in the posterior section.

The studies presented below investigate the ability of MCAs to move within the SCS and whether ARF is able to concentrate MCAs and improve the delivery of a fluorescent dye, which features as a stand in for a drug payload. Also described is an experimental technique for generating multilayer MCAs capable of carrying large payloads of therapeutic agents which could ultimately be used for delivering drugs within the eye or elsewhere in the body.

Explanation of role and format:

This thesis is divided into 3 main chapters. Chapters 1 and 3 are papers which have been published in peer-reviewed journals and to which I was a contributing author. Chapter 2 represents unpublished work which will be expanded on in the future for submission to a peer-reviewed journal and is my own project. For Chapter 1, my role was to collect and process ultrasound data, and to create images and videos. For Chapter 3, I was responsible for producing multilayer gas liposphere at UNC and the collection and analysis of ultrasound data and images.

Chapter 1.

Effect and distribution of contrast medium after injection into the anterior suprachoroidal space in ex vivo eyes†

Introduction

Diseases of the posterior segment of the eye are among the most common causes of blindness. In humans, these diseases include age-related macular degeneration, proliferative vitreoretinopathy, diabetic macular edema, and endophthalmitis. Although there are many advances in the treatment of these posterior segment diseases, the challenges of drug delivery to this part of the eye remain high.[28] Eye drops continue to be a mainstay in the treatment of ocular disease, but most topical medications do not penetrate the posterior segment.[37,38] Local therapy of the eye, such as periocular and intravitreal injections, has recently become popular to treat ocular disease because they minimize systemic side effects and take advantage of small tissue volumes and compartments of the eye.[39,40] Natural barriers to ocular drug penetration, such as conjunctival lymphatics, sclera, choroidal circulation, and epithelial tight junctions, limit the ability of periocular injections to reach posterior target tissues.[28,29,41] Instead, ocular posterior segment disease, such as choroidal neovascularization, macular degeneration, and retinal degeneration, are commonly treated locally by intravitreal or subretinal injections or use of sustained release devices. However, these treatment modalities are subject to complications such as injection site hemorrhage, retinal detachment, cataract formation, endophthalmitis,

_____

elevated intraocular pressure, opacities of the visual axis, and local toxicity. [30–32] Therefore, alternative sites for drug delivery to the ocular posterior segment are needed.

Drug delivery to the suprachoroidal space (SCS), a potential space located between the choroid and the sclera,[42] avoids many of the disadvantages of other local therapies by eluding barriers such as conjunctival lymphatics and the sclera and may avoid complications associated with intraocular injections or implants. Furthermore, because the SCS is adjacent to the entire choroid and thus the ocular posterior segment, drug delivery using the SCS has the potential for wide drug distribution and for reach to posterior target tissues.

Recently, studies have demonstrated promise in the use of the SCS as a site for drug delivery to the eye. Use of the SCS as a drug delivery site was first described by Einmahl et al.,[33] who placed a poly-ortho ester–sustained drug delivery system in the SCS in rabbits and demonstrated sustained delivery in the SCS for 3 weeks.[33] Ultrasound was used to track the distribution of injected material in this study.[33] In 2006, Olsen et al.[34] described the use of a fiberoptic microcannula to access the SCS in a pig with few complications.[34] Sustained ocular drug delivery of triamcinolone to the SCS was demonstrated using this cannula, with resulting low systemic drug levels. A volume of 12 µL triamcinolone was placed into the SCS by use of the flexible catheter, and no side effects were noted with the cannulation procedure or drug; after the cannula was removed, the SCS was found to return to a normal configuration.[34] Subconjunctival infusion (1 and 10 µL/min) of gadoliniumdiethylenetriaminopentaacetic acid (Gd-DTPA) in rabbits resulted in no ocular posterior segment distribution, whereas anterior intrascleral infusion resulted in rapid entry of Gd- DTPA into the SCS. The Gd-DTPA was then demonstrated to widely distribute to the posterior segment of the eye by way of the SCS.[41] In another study in rabbits, up to 100 µL fibrin glue was injected into the SCS, resulting in minimal

6

toxicity and complications.[43] Preliminary studies have also demonstrated that large biological

proteins, such as a human antibody (i.e., bevacizumab), injected into in the SCS in a pig model

resulted in no inflammation, whereas a similar dose injected intravitreally resulted in

granulomatous vasculitis and vitreitis.[44] Finally, the effectiveness of drug delivery to the SCS was

demonstrated in a study in which a sustained-release matrix-reservoir cyclosporine device that

was placed in the SCS resulted in long-term control of uveitis in a naturally occurring model of

autoimmune uveitis.[45] Therefore, the SCS route of delivery may offer a unique avenue for future

routine injections that are safe and effective in targeting retinal and macular diseases.

To further develop the SCS as a site for drug delivery, it is important to determine

whether injections of medications into the anterior SCS, the most accessible location of the SCS,

will allow distribution of the drug to the posterior targeted tissue. The SCS can be accessed

through a small sclerotomy or by microneedles placed 4 to 6 mm posterior to the limbus, but

the amount of drug distribution to the ocular posterior segment that can be achieved from this

anterior injection location is not known. Recently, Patel et al.[46] described the use of hollow

microneedles to precisely inject drugs into the SCS. In this study, volumes up to 35 µL prototype

drugs of particle sizes up to 1000 nm were injected into the porcine SCS. These injections

resulted in a 7% distribution to the posterior SCS.[46] However, appropriate injection volumes,

area of drug distribution, and effect on the SCS of injections must be further evaluated.

Furthermore, the duration of drug delivery and the ability of the drug to reach target tissues,

especially the retina, must be determined for each drug and formulation.

The purpose of this study was to evaluate injections into the anterior SCS to determine

the effect and distribution to the posterior SCS and to determine whether target tissues can be

reached. In this study, injection volumes, acute effects of injections on the SCS, and flow characteristics of injections in the SCS were determined.

Methods

Suprachoroidal Injection Technique

Adult porcine ex vivo eyes (Animal Technologies, Tyler, TX) were collected and shipped overnight on ice. Canine ex vivo globes were collected at a local animal shelter immediately after euthanatization and transported on ice. All globes were used within 24 hours of collection. Each globe was cleaned of excess periocular tissue, including conjunctiva, extraocular muscle, and orbital fat. Canine and porcine eyes are similar in size (e.g., canine vitreous humor volume is approximately 1.7 mL whereas porcine vitreous volume is slightly higher at 2.0 mL[47,48]), and, therefore, the procedures described are applicable to each type of eye. A 2-mm full-thickness scleral incision was made 5 mm posterior to the superior limbus to expose the SCS. A 27-gauge cannula (Anterior Chamber Cannula; BD Visitec, Waltham, MA) was placed 1 mm into the SCS through the scleral incision with the opening of the cannula directed posteriorly. Cyano-acrylate tissue adhesive (Pacer Technology, Rancho Cucamonga, CA) was used to seal the sclera incision and fixate the cannula to the external sclera.

Latex Distribution

Porcine and canine eyes were allowed to warm to room temperature for 30 minutes and then were injected with undiluted liquid anatomic latex (Carolina Biological Supply Company, Burlington, NC) through the 27-gauge cannula placed in the SCS. The liquid latex was injected until injection resistance developed or when disruption of the cyanoacrylate incision

seal and reflux of latex through the scleral incision occurred. An injection of approximately 1000 µL latex was required. Globes were then fixed in 10% buffered formalin (Fisher Scientific, Kalamazoo, MI) for 48 hours and sectioned either sagittally or in quadrants (i.e., flat mount) after removal of the ocular anterior segment. The retina and choroid were then removed, exposing the latex in the SCS and the sclera. High-resolution digital photographs (Nikon D200, AF-S DX Micro NIKKOR 85mm f/3.5G ED VR Lens; Nikon USA Inc, Melville, NY) of the eyes were analyzed using image analysis software (Elements 4.0, Adobe Photoshop, San Jose, CA; ImageJ software [developed by Wayne Rasband, National Institutes of Health, Bethesda, MD; available at http://rsb.info.nih.gov/ij/index.html]) to determine overall percentage area of distribution of latex to the entire SCS. Results were reported as mean (± SD) of percentage SCS distribution.

SCS Distension

Ex vivo canine and porcine eyes were used for this study. SCS cannulation was performed as described earlier. During the injection of 250, 500, 800, and 1000 µL (n = 6 eyes for each volume) of 0.9% phosphate-buffered saline (Fisher Scientific, Fair Lawn, NJ), high-frequency (50 MHz) ultrasound (E-technologies, Bettendorf, IA) was used to image the effect and distension of the injections on the SCS in real time. The ultrasound probe was positioned immediately over the injection site so that the adjacent sclera, SCS, and ciliary body/choroid were imaged in real time during the injection. Images were collected, and the maximal distance that the SCS was distended when injected with PBS was measured with internal calipers of the ultrasound. Results were reported as mean SD of SCS separation in millimeters of six eyes at each PBS volume. To determine the effect of physiologic intraocular pressure (IOP) on SCS distension after injection and to determine the changes of IOP after SCS injection, this study was

repeated in porcine ex vivo eyes (n = 4 per injection volume). After placement of the catheter in the SCS as described, a 27-gauge needle was placed through the limbus into the anterior chamber, and cyano-acrylate tissue adhesive was used to seal the limbal incision. The needle was connected with 0.9% saline-filled tubing to a pressure transducer (MedEx LogiCal Transducer, Model MX960; MedExSupply Medical Supplies, Monsey, NY) and an electronic monitor, allowing for continuous measurement of IOP. Immediately before injection of 250, 500, 800, or 1000 µL PBS into the SCS, the IOP was increased to 15 mm Hg by injection of 0.9% saline through the 27-gauge anterior chamber needle. Maximal distension of the SCS was measured and reported as described using internal calipers of the ultrasound. The IOP (in mm Hg) at the time of maximal SCS distension was recorded for each injection volume and reported as mean change in IOP (±SD) mm Hg.

Two-Dimensional Ultrasound Contrast Imaging of SCS

Porcine ex vivo eyes were used for this study. Using contrast-enhanced ultrasound (Mylab70; Biosound Esaote, Inc., Indianapolis, IN), 250, 500, and 800 L microbubble ultrasound contrast agent (Targestar-P, Targeson Inc., San Diego, CA) was injected into the anterior suprachoroidal space through 27-gauge cannulas placed as described earlier. In real time, observations were recorded, including flow characteristics of the contrast agent in the SCS. Percentage of maximal distribution in the SCS of contrast agent was determined in the sagittal ultrasound plane using image analysis software (Elements 4.0 [Adobe Photoshop]; ImageJ 1.42q). Results were reported as mean (± SD) of percentage SCS distribution of four eyes at each contrast agent volume. Using contrast medium detection software (Qontrast; Biosound Esaote,

Inc., Indianapolis, IN), regions of interest were placed over the entire SCS and the posterior SCS, and contrast enhancement over time was measured as mean pixel intensity.

Three-Dimensional Ultrasound Contrast Imaging of SCS

Porcine ex vivo eyes were imaged using a custom 3D contrast imaging system that interfaces a computer-controlled linear motion axis with a clinical ultrasound scanner (Acuson Sequoia; Siemens Medical Solutions, Malvern, PA). A 4-MHz (4-C1) transducer and contrast imaging (Cadence CPS; Siemens Medical Solutions, Malvern, PA) were used. The porcine eye was placed in a water bath, and 250 μL microbubble IOVS, July 2011, Vol. 52, No. 8 Contrast Ultrasound of the Suprachoroidal Space 5731 contrast medium was injected through 27-gauge catheters placed into the anterior SCS. Dynamic contrast medium inflow was observed in a midsagittal plane, followed by 3D imaging of the entire globe to assess spatial distribution of the contrast agent. Percentage of maximal distribution in the SCS of contrast agent was determined slice by slice using image analysis software (Elements 4.0 [Adobe Photoshop]; ImageJ 1.42q). Results were reported as mean (SD) of percentage SCS distribution of 4 eyes.

Statistical Analysis

Statistical analysis of the data was performed using computerized software (JMP Statistical Discovery Software, vs 8.0; SAS Inc., Cary, NC). Differences in SCS distension, distribution of latex, distribution of contrast media, and contrast medium enhancement were analyzed using analysis of variance (ANOVA) with Tukey's HSD test. Differences between species were analyzed using an unpaired t-test. Significance was set at $P < 0.05$ for all comparisons.

Results

Latex Distribution

Liquid anatomic latex was injected into the anterior SCS to determine posterior distribution from a single anterior injection. In canine eyes, latex distributed to a mean (± SD) of 39.9% ± 5.2% of the entire SCS on sagittal sections (n = 4) and 46.8% ± 13.1% of the entire SCS when the eyes were sectioned in quadrants (n = 4; Fig. 1). In porcine eyes, latex distributed to a mean (± SD) of 54.8% ± 15.4% of the SCS in sagittal sections (n = 4) and 42.1% ± 4.3% of the SCS in eyes sectioned in quadrants (n = 4; Fig. 1). There were no significant differences between species or sectioning techniques in area of distribution. Latex reached the SCS adjacent to the area centralis (i.e., macula) in 9 of 16 (56%) eyes (Fig. 1).

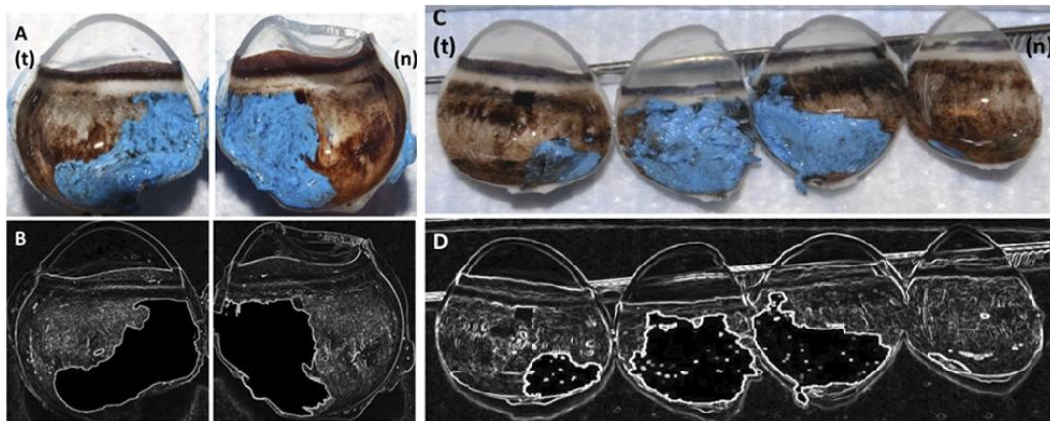**Figure 1.** Temporal (t) and nasal (n) sagittal sections of a canine globe showing the suprachoroidal distribution of a single injection of blue latex in color (**A**) and in the "edges" function of ImageJ software (**B**). Canine globe sectioned in quadrants demonstrating distribution of blue latex in the SCS in color (**C**) and in the "edges" function of ImageJ software (**D**).

SCS Distension

High-frequency ultrasound was used to image the anterior SCS during injection with PBS. The metallic tip of the catheter was visualized in the SCS on the ultrasonic image. On injection, the SCS rapidly expanded locally, then dissected posteriorly (Fig. 2). As expected, the lower volumes of injection resulted in less distension of the SCS. In the canine eyes, maximum mean (± SD) distension of the SCS from injection with 250 µL PBS (1.25 ± 0.07 mm) was significantly lower than the maximum distension created from 500 µL PBS (2.25 ± 0.07 mm; $P < 0.02$), 800 µL PBS (2.25 ± 0.21 mm; $P < 0.02$), and 1000 µL PBS (2.7 ± 0.28 mm; $P < 0.005$; ANOVA with Tukey's HSD; Fig. 3). In the porcine eyes, maximum mean (± SD) distension of the SCS from injection with 250 µL PBS (1.57 ± 0.48 mm) was significantly lower than the maximum distension created from 800 µL PBS (2.98 ± 0.37 mm; $P < 0.002$), and 1000 µLPBS (3.28 ± 0.57 mm; $P < 0.0002$). Furthermore, the mean distension of the SCS from injection with 500 µL PBS (2.57 ± 0.52 mm) was significantly lower than the mean distension created from 1000 µL PBS ($P < 0.036$; ANOVA with Tukey's HSD; Fig. 3). There were no significant differences in distension of the SCS between canine and porcine eyes at any injection volume except 800 µL, at which the distance was significantly greater in the porcine eye (2.98 ± 0.37 mm) than in the canine eye (2.25 ± 0.21 mm; $P < 0.035$; Student's t-test; Fig. 3).

To determine the effect of physiologic intraocular pressure (IOP) on SCS distension after injection and to determine the changes of IOP after SCS injection, this study was repeated in porcine ex vivo eyes with IOPs of 15 mm Hg. In these eyes, there was no significant difference in mean (± SD) distension of the SCS between (eyes injected with 250 µL (1.65 ± 0.79 mm), 500 µL (2.8 ± 0.69 mm), or 800 µL (2.8 ± 0.92 mm; Fig. 3). There also were no significant differences in mean distension for each injection volume between eyes with IOPs at 15 mm Hg compared with the ex vivo porcine or canine eyes (Fig. 3). However, injections greater than 800 µL could not be completed because of resistance to injection from high IOPs. In fact, at maximum distension

13

during the injection of 250 µL, IOPs were transiently (<10 seconds) elevated a mean (± SD) of

39.3 ± 16.5 mm Hg; during the 500-µL injection, IOP increased a mean (± SD) 189.5 ± 118.1 mm

Hg; and during the 800-µL injection, IOP increased a mean (± SD) 285.8 ± 42.9 mm Hg.
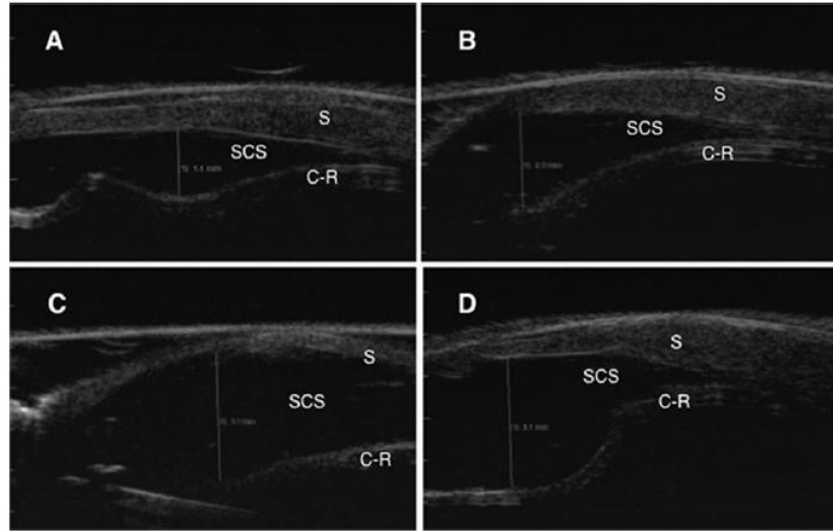

Figure 2. High-frequency ultrasound (50 MHz) images demonstrating the distension of the SCS in porcine eyes after injection with 250 µL (A), 500 µL (B), 800 µL (C), and 1000 µL (D) of PBS. Left: anterior segment; right: posterior segment. S, sclera; C-R, choroid and retina.
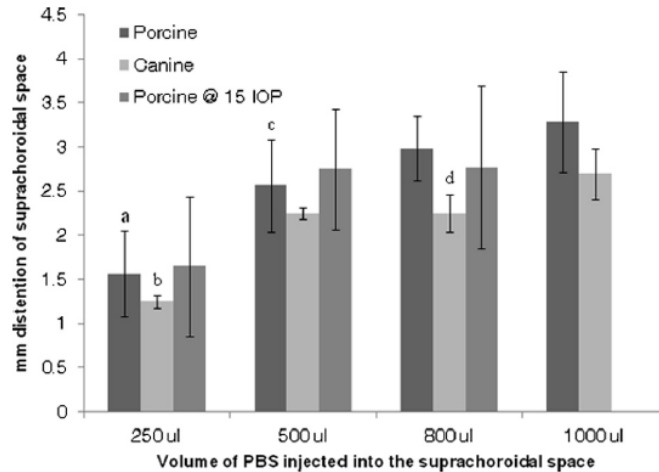
Figure 3. Mean ± SD distension of the SCS after injection with PBS measured using high-frequency (50 MHz) ultrasound of *ex -vivo* porcine eyes (porcine; n = 6), canine eyes (canine; n = 6), and porcine eyes with IOP at 15 mm Hg (porcine at 15 IOP; n = 4). (a) Porcine eyes; mean (± SD) distension of the SCS from injection with 250 μL PBS was significantly less than the maximum distension created from 800 μL PBS (P = 0.002) and 1000 μL PBS (P = 0.0002). (b) Canine eyes; mean (± SD) distension of the SCS from injection with 250 μL PBS was significantly less than the mean distension created from 500 μL PBS (P = 0.02), 800 μL PBS (P = 0.02), and 1000 μL PBS (P = 0.005). (c) Porcine eyes; mean distension of the SCS from injection with 500 μL PBS was significantly less than the mean distension created from 1000 μL PBS (P = 0.036). (d) Mean distance was significantly less in the canine eye than in the porcine eye for the 800-μL PBS injection volume (P = 0.035; Student's t-test). There was no significant difference in mean distension of the SCS in porcine eyes at 15 mm Hg compared with the other *ex-vivo* eyes at any injection volume.

Two-Dimensional Ultrasound Contrast Imaging of SCS.

After the injection of microbubble ultrasound contrast agent into the anterior SCS of porcine eyes (n = 4 eyes per volume), contrast was visible initially in the SCS at the injection site and then at the opposite ventral anterior SCS and the posterior SCS. This is illustrated in Figure 4, where contrast enhancement (measured as mean pixel intensity) starts to increase first at the injection site, followed by the opposite anterior SCS and the posterior SCS. The overall mean (± SD) time after injection for contrast to appear at the opposite and posterior SCS was 7.8 ± 4.6 and 7.7 ± 4.6 seconds, respectively. This suggests that the contrast flowed in the SCS initially

15

parallel to the limbus in the anterior suprachoroidal space as it extended posteriorly (Fig. 5;

Supplementary Movie S1,http://www.iovs.org/lookup/suppl/doi:10.1167/iovs.11-7525/-/DC

Supplemental). Mean (± SD) time to maximum contrast intensity visible in the SCS on the

ultrasound image was 16.2 ± 4.6 seconds after injection. There were no significant differences

among 250-, 500-, and 800-μL contrast volumes injected in time after injection to appearance of

the contrast on the ultrasound image (Table 1). In the sagittal ultrasound section, the

microbubble contrast agent was visible in a mean 24.0% to 27.2% of the entire SCS when

injected with 250, 500, or 800 μL microbubble contrast agents (Table 1). There were no

significant differences in area of the SCS where contrast agent was visible among the three

volumes injected (P = 0.90) or in mean pixel intensity of contrast medium (P = 0.35; Fig. 6).

Despite only approximately 25% of the SCS having visible contrast, 10 of 12 eyes (83.3%)

injected had contrast that reached the posterior pole of the eye (one 250-μL and one 800-μL

injection did not, but contrast was observed to extend to approximately two thirds of the

posterior SCS).
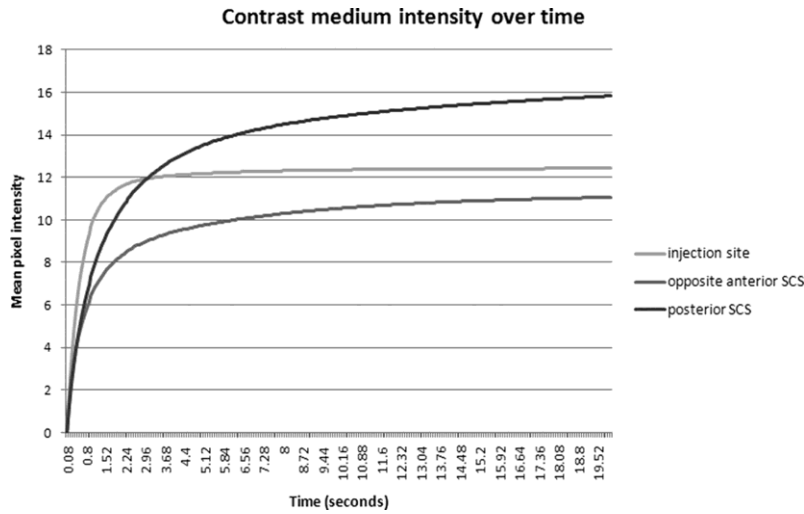
Figure 4. Mean pixel intensity representing contrast medium enhancement in regions of interest placed over the injection site, opposite the anterior SCS and the posterior SCS after injection of 250, 500, and 800 µL microbubble contrast agent into the superoanterior SCS of an *ex-vivo* porcine eye. Measurements of all contrast medium doses are combined in this graph. Contrast enhancement increases rapidly at the injection site, followed by the opposite anterior and posterior SCS.

Volume of Ultrasound Contrast Injected	Time to Opposite Anterior SCS (s)	Time to Posterior SCS (s)	Distribution of SCS (%)	Extension to Posterior Pole
250 µL	12.3 ± 5.9	4.3 ± 1.5	24.0 ± 9.3	3 4 eyes
500 µL	6.0 ± 4.1	9.5 ± 6.0	24.6 ± 9.2	3 4 eyes
800 µL	6.3 ± 2.1	8.5 ± 3.9	27.2 ± 13.2	4 4 eyes
Overall	7.8 ± 4.6	7.7 ± 4.6	25.3 ± 9.8	10 12 eyes

Values are mean +/- SD.

Table 1. Two-Dimensional Ultrasound Evaluation of the SCS Using Microbubble Contrast

Three-Dimensional Ultrasound Contrast Imaging of SCS.

As described for 2D ultrasound imaging, in 3D imaging (n 4 eyes) microbubble contrast medium first appeared in the SCS at the injection site, then moved to the opposite side of the anterior SCS and into the posterior segment. Contrast agent was uniformly distributed in the anterior SCS, and reached the posterior SCS in all eyes (Fig. 7; Supplementary Movie S2, http://www.iovs.org/lookup/suppl/doi:10.1167/ iovs.11-7525/-/DCSupplemental). Median percentage of contrast agent distribution in the entire SCS was 45.3%, with a range of 39.0% to 52.1%.
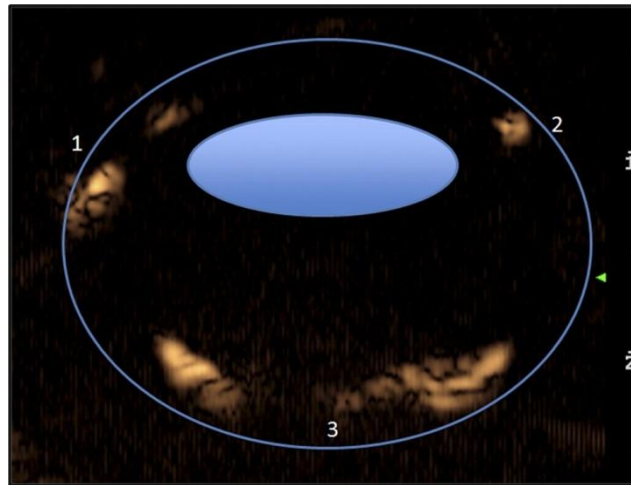
Figure 5. Ultrasound image, with overlay of basic ocular schematic, after injection of 500 μL microbubble contrast agent into the superoanterior SCS of an *ex-vivo* porcine eye. Contrast was visible inititally in the SCS at the injection site (1), then visible at the opposite ventral anterior SCS (2) and the posterior SCS (3). An ultrasound system with contrast imaging capabilities was used to image the eye.

Discussion

A single injection into the anterior SCS resulted in the distribution of latex to nearly 50% of the ocular posterior segment in two large animal species commonly used for retinal research. The SCS was demonstrated to be able to expand, in a dose dependent manner, to accommodate

various volumes of injected fluid. Physiologic IOP did not affect the distension of the SCS after injection, but there was a dose-dependent transient increase in IOP after injection. The clinical and pathologic significance of this transient increase in IOP must be further investigated; however, injections of 500 and 800 L in eyes with physiologic IOP resulted in acute pressure elevations likely sufficient to damage retinal ganglion cells or the optic nerve.[49,50] The results of this study also demonstrated that it is possible to image the SCS with an ultrasound contrast agent. Furthermore, these results support our hypothesis that a single anterior suprachoroidal injection of a drug with a volume as low as 250 L can reach the ocular posterior segment in eyes that approximate the size and volume of the human eye. Together our results suggest that injections of 250 L or less can be accommodated by the SCS, result in only transient relatively modest elevations of IOP, and rapidly extend to a large percentage of the ocular posterior segment. Therefore, further development of SCS injections for treatment of macular disease and other diseases of the posterior segment of the eye is warranted.

Our results are similar to the results from a recent study of the injection of particles into the SCS of *ex-vivo* rabbit eyes. Using specific microneedles, a 15-L volume of microparticles injected into the anterior SCS resulted in distribution of the particles to approximately 36% of the total circumference of the eye.[51] However, in porcine *ex-vivo* eyes, 35 L barium sulfate contrast agent particles resulted in only approximately 7% posterior segment distribution, as determined with reconstructed MRI images.22 Therefore, higher SCS injection volumes, as used in our studies, may be required for adequate posterior distribution of medication in larger eyes. What effect these large injection volumes had on the *in-vivo* eye remains to be determined. However, it has been demonstrated that the *in-vivo* rabbit eye can accommodate SCS injections of up to 200 L sodium hyaluronate or perfluorocarbon gases.[52,53] Therefore, it is likely that the

larger canine, porcine, or human eye would also tolerate SCS injection volumes capable of large (200–250 L) posterior segment distribution.

This study demonstrates that contrast-enhanced ultrasound can be used to determine the dynamic distribution of a single anterior SCS injection in real time. Ultrasound contrast agents are composed of a perfluorocarbon gas core encapsulated by a lipid shell, stabilized by a layer of polyethylene glycol. The microbubbles are suspended in saline at a concentration of approximately 1×10^9 particles/mL, with a median bubble diameter of approximately 2.5 μm.[25] Ultrasound contrast agents may not accurately reflect the flow and distribution of drugs in the SCS because of differences in particle size and viscosity. Microbubbles, because of their gas content, tend to rise to the upper portion of a fluid-filled space, which could alter the distribution of the contrast agent in the SCS when compared with injected medication. However, the porcine eyes in this study were imaged with the anterior SCS facing up, which might have led to an increased accumulation of microbubbles in the anterior SCS and a non–gravity-dependent liquid would be expected to reach the posterior SCS even better. The fact that the ultrasound contrast agent consistently reached the posterior segment is very encouraging for the development of SCS injections for the treatment of ocular posterior segment diseases.

Contrast flow, when observed dynamically in a midsagittal image plane, extended from the injection site in the anterior SCS to the contralateral anterior SCS, indicating flow parallel to the limbus in the anterior SCS. Simultaneously, or in some eyes with a small delay, contrast medium also extended to the posterior SCS. In all eyes the posterior segment was reached by the contrast agent within seconds, confirming that the SCS can be used as a site for drug delivery and that injections of medications into the anterior SCS, the most accessible location of

20

the SCS, will allow distribution of the drug to the posterior targeted tissue. Viscous or microparticle formulations may have different distribution characteristics, but our preliminary studies with latex, PBS, and ultrasound contrast demonstrated rapid distribution into the posterior SCS.

The ability of ultrasound contrast agents to reach the posterior segment of the eye is not only of value when considering the anterior SCS as a site for therapeutic drug administration, it may also be a method for specific drug delivery. Contrast ultrasound-assisted drug delivery has been shown to be feasible both *in-vivo* and *in-vitro*.[55] Binding of pharmaceutical agents to the microbubble shell turns the contrast agent into a vehicle for drug or gene delivery.[56,56] Moreover, a higher energy ultrasound beam can be applied focally in the targeted region, such as the macula, to disrupt microbubbles and cell membranes and locally deliver the drug or gene, thus avoiding the systemic distribution of the substance and potentially reducing the blood-ocular barrier.[14,58]

Three-dimensional contrast-enhanced ultrasound is a novel technology that allows understanding of the pattern of distribution
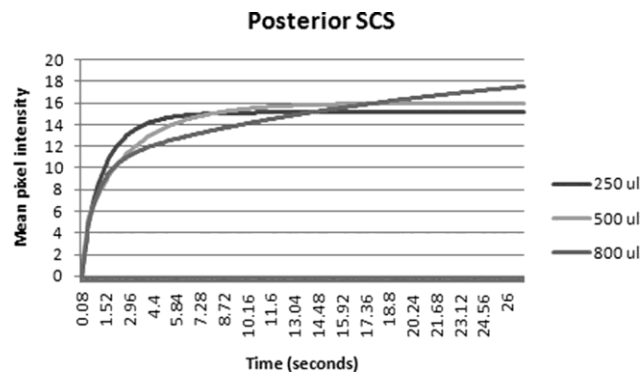
Figure 6. Mean pixel intensity representing contrast medium enhancement in regions of interest placed over the posterior SCS after the injection of 250, 500, and 800 L microbubble contrast agent into the superoanterior SCS of an *ex-vivo* porcine eye. No significant differences in contrast medium enhancement were detected with different doses (P = 0.35).
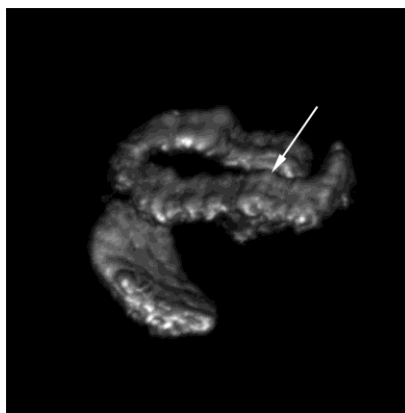
Figure 7. Three-dimensional model of contrast agent distribution within the eye. Microbubble contrast agent (250 L) was injected into the superoanterior SCS of an *ex-vivo* porcine eye, and 3D ultrasound was performed. The contrast agent in the SCS is isolated in this image; no other structures are displayed. The corneal surface faces up in this image. Arrow: injection site.

of contrast medium in the SCS. Selecting a single two dimensional image, or even multiple two-dimensional images, for measuring the percentage distribution of contrast agent is prone to underestimation or overestimation of the actual distribution because of the variability of contrast flow within the SCS.[59] This may explain the higher percentage of contrast medium distribution when considering 3D imaging of the entire eye compared to a single slice; 3D imaging was limited to the lowest volume of 250 L because no statistically significant differences in contrast distribution were detected with 2D imaging performed with different volumes.

These studies represent a novel approach for performing and assessing injections into the anterior SCS and suggest that access to the anterior SCS, either by cannula or microneedles, may allow the distribution of drugs to a large area of the ocular posterior segment and to the macular area of the eye. Additional studies are needed to determine the effect of choroidal

blood flow and IOP on the distribution of specific medications and formulations to the retina

and macula. Furthermore, contrast ultrasound-assisted drug delivery from SCS injections may

represent a novel, targeted, and less invasive method of treatment of ocular posterior segment

disease.

CHAPTER 2.

Effect of acoustic radiation force on distribution of fluorescent dye after injection into the anterior suprachoroidal space in *ex vivo* Eyes

Introduction

Microbubble contrast agents (MCAs) are widely used for enhancing blood flow imaging in diagnostic ultrasound,[36] and are the target of investigation for a wide number of uses in therapeutic applications.[11,13,16-17] These contrast agents are micron-sized gas filled bubbles, typically encapsulated in a stabilizing shell of phospholipid, protein or polymer.[3] The inner core is filled with a high molecular weight or low solubility gas such as perfluorocarbons or sulfahexafluoride,[36] though cheaper gasses such as nitrogen can be used at the cost of decreased stability. During *in vivo* use, MCAs are introduced to the blood stream, typically through a peripheral venous injection, and circulate within the vascular network. Due to their size, they remain confined to the vascular space and are not able to diffuse across the endothelial layer.[3] Because of the large acoustic impedance mismatch between tissue (including blood) and the gas core of the bubbles, MCAs reflect a significant amount of energy back toward the imaging probe. The non-linear response of MCAs during acoustic oscillation enable the application of specific imaging strategies to suppress signal from tissue which enhances imaging of the vascular space.[5]

In the presence of an ultrasound field, MCAs experience a net force in the direction of wave propagation, which will cause displacement of the bubbles.[22] Additionally, groups

of bubbles experience a net attractive force under the same conditions.[23] These effects have been termed primary acoustic radiation force (ARF) and secondary ARF respectively. This phenomenon has been shown to increase MCA concentration *in vivo*. While the overall force is small, it is enough to displace MCAs out of the central blood flow in a high flow velocity vessel. It has been shown that the ARF strength is dependent upon both bubble size and frequency of the insonifying wave.[60] Radiation force is maximized when the frequency of the ultrasonic wave matches the resonant frequency of the MCA.[60] Bubble disruption and destruction occur when an ultrasonic pulse of sufficient pressure is applied to the bubble. Large oscillations of the bubble allow rupturing of the encapsulating shell and diffusion of gas into the surrounding liquid causing the loss of echogenicity.[3]

To facilitate both diagnostic and therapeutic applications, MCAs have been designed to carry markers or other drugs within or on their surface.[13-15] Attaching ligands or antibodies to the surface of MCAs allow them to specifically target diseased tissues or other areas of interest.[18,19] Drugs may be directly incorporated into the shell[13] or interior of MCAs[26], or conjugated to the shell as nanoparticles.[14] Destruction of MCAs at specific sites within the body can thus result in the targeted release of these therapeutic molecules.

The majority of current ultrasound transducers provide imaging information in a two dimensional plane. While there are transducers available that provide full three dimensional (3D) volumetric data, they are not wide spread and have limited functionality for contrast specific applications. Traditional probes can be used to capture volumetric data sets by acquiring multiple images through a volume in a series of parallel slices.[18] Mechanical scanning is the most repeatable way to fully interrogate a 3D sample of tissue using a linear array.[59]

Diseases occurring in the posterior portion of the eye are a leading cause of blindness. These include diabetic macular edema, proliferative vitreoretinopathy, age-related macular degeneration and endophthalmitis. While many advancements have been made in treating these diseases, delivering drugs to the affected regions remains a challenge. Topical treatments, such as eye drops, often fail to reach the posterior segment.[28] Intravitreal and subretinal injections provide the ability to overcome this limitation but are associated with complications including injection site hemorrhage, retinal detachment, the formation of cataracts, elevated intraocular pressure and opacities of the visual axis.[30-32] The suprachoroidal space (SCS) offers a possible alternative for delivering drugs to posterior portions of the eye. The SCS is a virtual space between the sclera and choroid which previous studies have shown allows access from the anterior segment to the posterior segment of the eye. Drugs injected into the SCS avoid the barrier of the sclera and can potentially reach targets throughout the globe and may avoid complications associated with more invasive injection techniques. Use of the SCS for drug delivery first described by Einmahl et al.,[34] and the technique has since been used by a number of researchers.[40,41,44]

The goal of the current study is to determine if the application of ARF to microbubbles injected into the SCS will increase the posterior localization of a fluorescent dye.

Methods

3D ultrasound using linear motion stage

To perform 3D ultrasound using a linear array ultrasound probe, a linear motion stage from Newport (UTS150PP - Newport, Irvine, CA) was used. The motion stage was controlled using a motion controller (SMC100 – Newport, Irvine, CA). The motion stage and

26

controllers were interfaced to a PC using LabVIEW software (National Instruments, Austin, TX). Using this equipment, the ultrasound transducer could be scanned in a controlled fashion along the elevational dimension to fully sample a 3D volume.

Ultrasound System

A Mylab 70XVG with LA 332E transducer (Biosound Esaote North America – Indianapolis, IN) was used for all experiments. The system and transducer include a contrast specific imaging mode which was used for all ultrasound data acquisition. The built-in "Burst" sequence was used for MCA destruction. Since the ultrasound system used for this study does not have a built in ARF mode, it was required to determine what existing mode would provide the best parameters for producing ARF. Continuous Wave (CW) was chosen, because it would best approximate the large number of cycles needed to produce translation of the MCAs. To examine the output of the system in this mode, a needle hydrophone (HNA 0200 – Onda, Sunnyvale, CA) was positioned in a water bath with the transducer and the pressure output monitored with a digital oscilloscope. CW parameters including power, depth, pulse repetition frequency (PRF) and gate size were all varied in order to maximize the number of cycles output. For application of ARF to eyes the gate size was set to 24 mm and placed in the far field, the PRF set to 15 KHz and the frequency set to 6.3 MHz.

Formation of MCAs

MCAs were formulated with a lipid solution in a 9:1 molar ratio as previously described.[61] To create fluorescent MCAs, DiI (Vybrant DiI, Invitrogen - Eugene, OR) was incorporated at a concentration of 2 µL per 1.5 mL of lipid solution and stirred using a vortex mixer. The lipid solution was then mechanically agitated for 45 s. After agitation, MCAs were diluted into 10 mL of phosphate buffered saline (PBS) and washed via centrifugation (5 mins at 3000 rpm) to separate any dye which was not incorporated into the lipid shell of MCAs. The MCAs concentrated after centrifugation were diluted into 4 mL of PBS for a final concentration of approximately 7×10^9 bubbles/mL.

Suprachoroidal injections and Imaging

Ex-vivo adult pig eyes were collected (NCSU DVM - Raleigh, NC) and trimmed of excess adnexal tissue. Injections into the anterior portion of the SCS were made using microneedles (Clearside Biomedical – Atlanta, GA) designed to penetrate through the sclera without puncturing into the choroid. Each globe was injected with 150 µL of MCAs before ultrasound imaging began.

Eyes were covered in ultrasonic gel to allow acoustic coupling to the ultrasound transducer. A baseline 3D elevational scan was performed in contrast mode to observe the distribution of contrast medium after injection. The ultrasound system was then set to CW mode in order to deliver ARF and 3 elevational scans were taken across the eye to apply ARF, with the transducer moved laterally between each scan. After ARF was applied, a second contrast scan was taken to observe the distribution of contrast agents after application of ARF. Next, a slow scan across the eye was initiated with the ultrasound

system in "Burst" mode to destroy MCAs within the globe. Finally, a background elevational scan was taken to allow subtraction of any nonlinear signal that was present in the absence of contrast agents. Ultrasound data was exported from the system as AVI videos and analyzed offline using Image J (NIH- Bethesda) and Matlab (Mathworks - Natick, MA). Regions of interest (ROIs) were applied to the 3D ultrasonic data to separate the anterior, central and posterior portions of the eye. The total ultrasound intensity in each region was measured before and after application of ARF (Figure 9).

Dissection of eyes and DiI measurements

Eyes were set aside for 5 minutes to allow DiI to move throughout tissue, they were then frozen on dry ice before being dissected. Eyes were kept frozen during dissection with a cooled ceramic tile above dry ice and 2-methylbutane. The eye was first divided into 3 parts via 2 cuts along the coronal plane: an anterior section including the lens, a midsection and a posterior section. Each of these sections was then separated by tissue type into vitreous, retina, choroid, and sclera. To prevent transfer of DiI between samples, the surgical instruments were rinsed using PBS followed by methanol followed by PBS and then blotted dry. Samples were stored at -80°C until fluorescence measurements were made.

The ocular tissues were added to 0.5 mL of isopropanol (Acros organic - Fairlawn, NJ) and shaken with an orbital shaker (Fisher Scientific – Suwanee, GA) for 15 minutes. The aqueous layer was separated out by centrifuging the sample for 10 minutes at 10,000 g. The supernatant was analyzed using a spectrofluorometer (Flouroskan Ascent Fl, Thermolabsystem - Helsinki, Finland) using an excitation wavelength of 530 nm and an emission wavelength of 590 nm. A standard solution of DiI with a concentration range of 5

ng/mL to 3 µg/mL was prepared in isopropanol to calibrate the system. Student's T-tests

were used to compare results from each section using Excel (Microsoft – Redmond, WA).

Results

Radiation Force Output

The Esaote system was not able to deliver an ideal pulse for ARF within the

parameter ranges tested. At the most effective setting of 6.3 MHz, the largest duty cycle

output was 5% at 17.5 KHz and the ultrasound beam was narrowly focused to a -6 dB width

of approximately 5 mm. Though the translational speed of MCAs was not directly measured

under these settings, previous studies using similar parameters[23,24] indicated that bubble

velocities of 1 mm/s should be expected .

Distribution of contrast agents after ARF

3D ultrasound images of contrast medium in the eye both before and after the

application of ARF by the Esaote system showed no effect on distribution. Overall there was

a slight reduction in contrast signal after application of ARF. This is most likely due to some

destruction of MCAs during the application of ARF as the pressure in the center of the beam

(2.4 MPa, MI = 0.95) was high enough to destroy small MCAs.
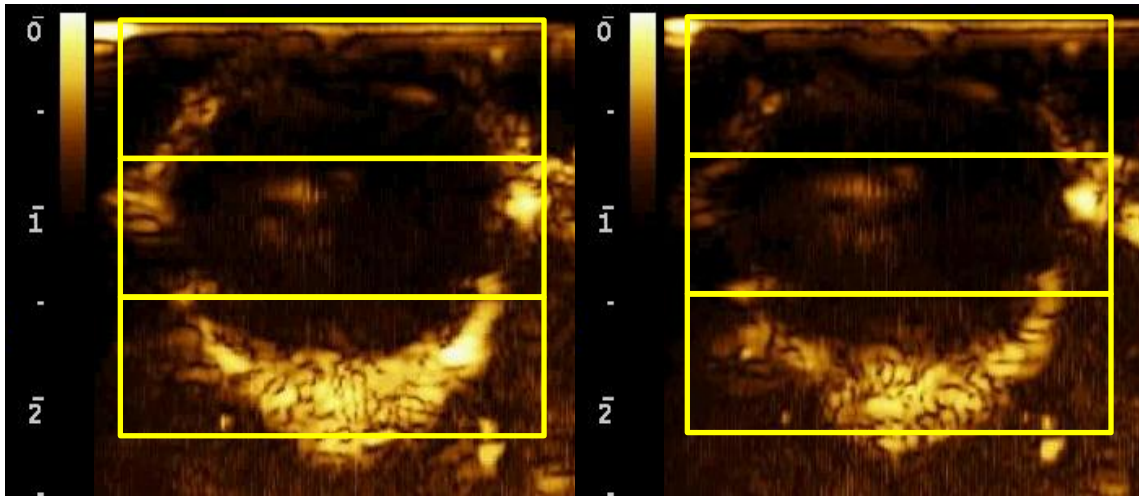
Figure 8. Ultrasound contrast image from central slice of eye showing the three ROIs used: anterior (top) center (middle) and posterior (bottom) before and after application of ARF. A) Before application of ARF. B) After application of ARF
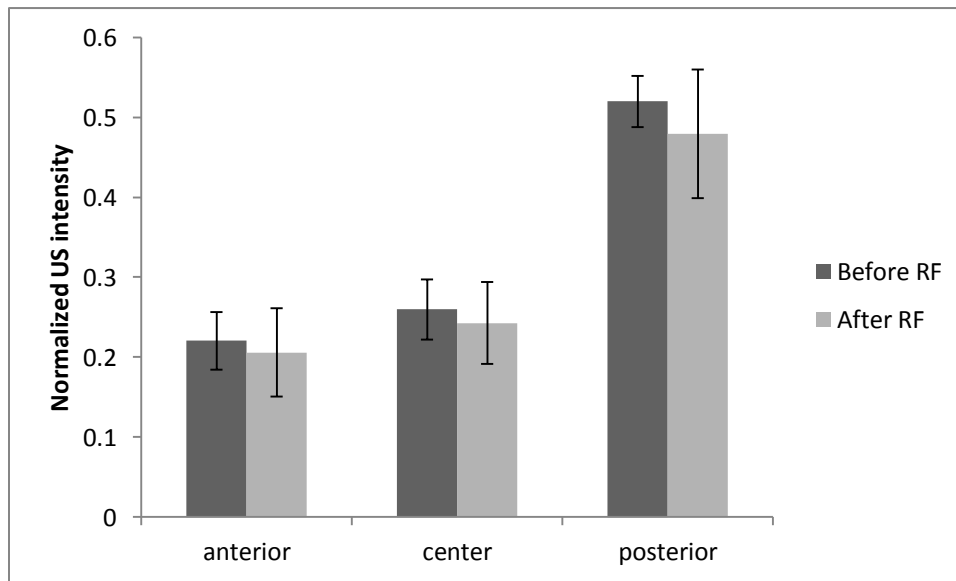
Figure 9. Ultrasound image intensity for each ROI in the eye, before and after application of ARF (n = 6). Images were collected across the entire 3D volume of the globes and ROIs applied for each captured image slice. Data shown are the summed ultrasound intensity across each ROI for the entire 3D volume.

Distribution of DiI with and without ARF

Measurements of DiI concentration within the various tissues showed highly variable results. In 54.5% of tissue samples, the concentration of DiI was below the measurement threshold of the spectrofluorometer. In the remaining samples, the concentrations ranged from 2 to 275 ng/g tissue. The total concentration of dye detected in each eye varied from 110.9 to 712.3 ng/g (average 281.3, stdev 139.5). This variation in concentration could not be accounted for by differences in eye mass.

The measured concentration of DiI in each tissue section is provided below.

	Vit	Ret	Cho	Scle
1 ANT	0	0	62.5	176
1 MID	2.6	15	116	10.2
1 POST	25	20	275	10
2 ANT	2.27	0	40	16.6
2 MID	2.6	0	75	40
2 POST	0	0	50	2.89
3ANT	0	66	150	15.62
3 MID	0	0	0	18
3 POST	0	0	0	3.12
4 ANT	3.96	0	200	28.12
4 MID	3.26	0	100	18.5
4 POST	16.6	27.2	125	4.3
5 ANT	11.8	0	66.66	25.8
5 MID	3.9	0	83.3	36.36
5POST	5	27.7	100	5.9
6 ANT	6.75	0	116.6	37.5
6 MID	0	27.7	125	28.5
6 POST	5.43	0	0	7.5
7 ANT	0	0	0	18.5
7 MID	7.6	108	83	20.8
7 POST	13	0	0	6.5
8 ANT	0	0	66.5	28
8 MID	0	0	0	30.9
8 POST	0	33	0	5.4
9 ANT	0	111	50	21.8
9 MID	0	0	0	26
9 POST	0	0	0	5.71
10 ANT	0	87	58	21
10 MID	0	0	0	33.3
10 POST	54.4	0	0	4.5
11 ANT	0	0	66.66	25
11 MID	0	0	0	31.5
11 POST	0	0	0	6.25
12 ANT	0	0	112.5	39.4
12 MID	0	0	0	28.9
12 POST	0	0	0	5.22

Table 2. DiI concentrations measured by spectrofluorometry for 4 tissue types in the ARF treated eyes, units of ng DiI/g tissue.

	Vitreous	Retina	Choroid	Sclera
7 ANT	3.03	0	100	35
7 MID	2.06	0	0	16.1
7 POST	1	0	0	3.73
8 ANT	3.4	0	66	29
8MID	0	0	0	7.8
8POST	0	0	0	4.7
9ANT	2.22	0	87.5	31.25
9 MID	2.5	35	0	48.6
9 POST	0	0	0	3.42
10 ANT	3.9	0	62.5	31.25
10 MID	0	0	75	30.5
10 POST	0	0	1	4.22
7 ANT	0	0	70	28.2
7 MID	0	0	0	39.47
7 POST	0	22	83	6.3
8 ANT	0	0		55
8MID	0	0	100	40
8POST	0	0	0	5.7
9ANT	4.25	0	58	38
9 MID	0	0	125	50
9 POST	0	0	62.5	9.18
10 ANT	0	0	112.5	38
10 MID	0	0	175	4.11
10 POST	0	0	100	8.69
11 ANT	0	41.6	90	50
11 MID	0	0	50	26
11 POST	0	0	83	5.76
12 ANT	0	0	75	40
12 MID	0	0	0	22
12 POST	0	0	100	30

Table 3. DiI concentrations measured by spectrofluorometry for 4 tissue types in the control eyes, units of ng DiI/g tissue.

Use of radiation force did not produce any changes in the relative distribution of fluorescence signal in the anterior portion of the eye compared to the entire eye (p = 0.74) or the posterior portion of the eye versus the whole eye (p = 0.89) as seen in Figure 10.
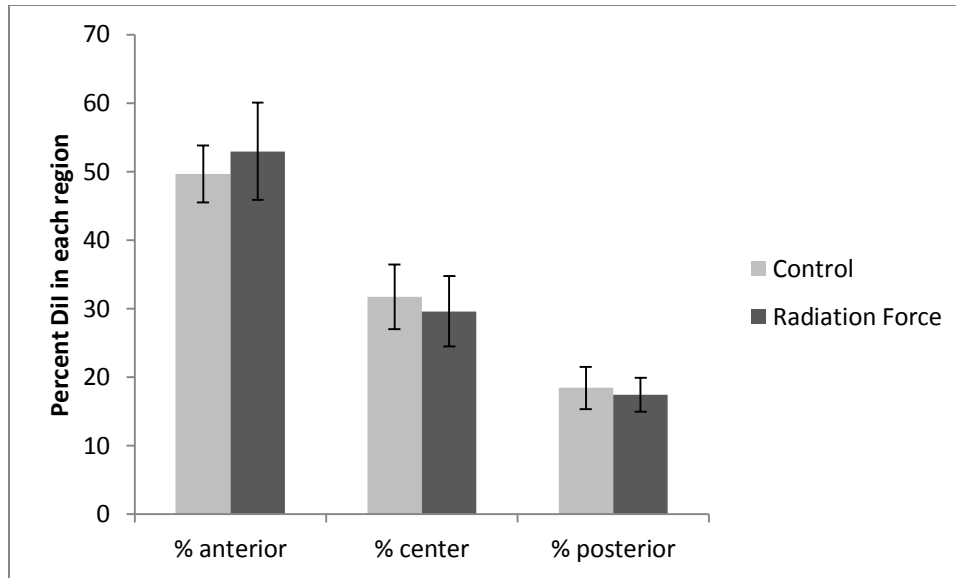
Figure 10. Percent of DiI residing in each region of the eye as compared to the whole eye for controls (n = 10) and ARF treated (n = 12). Most dye was concentrated in the anterior portion of the eye was contrast agents were injected. Treatment with ARF had no effect on dye distribution.

Analysis showed that significantly more dye resided in the choroid and sclera than the vitreous and retina. Since both choroid and sclera are adjacent to the SCS this finding is consistent with the physical layout of the eye. Concentrations were next highest in the retina, which can be reached by passing through the choroid. Concentrations in the vitreous were the lowest.

There was a statistically significant difference in the concentration of dye in the retina ($p = 0.04$) and in the vitreous ($p = 0.03$) between the ARF treated group (n = 12) and the control group (n = 10). No such difference existed in concentrations for the choroid and sclera (Figure 11).
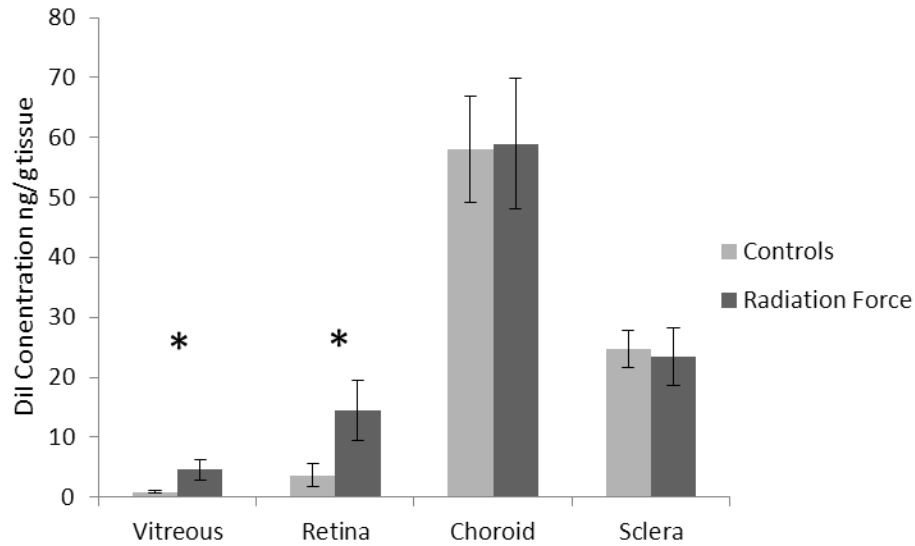
Figure 11. Concentrations of DiI in each anatomical tissue ng of DiI/gram of tissue for control eyes (n = 10) and ARF treated eyes (n = 12). Treatment with ARF caused significantly increased concentrations in the vitreous (p = 0.03) and in the retina (p = 0.04).

Discussion and future work

Acoustic radiation force parameters

Because the ARF beam used on the Esaote machine was much more tightly focused than the size of an eye, it was difficult to achieve a balanced intensity that was not destructive but was effective for pushing. The compromise reached was to lower the center pressure; however, this required that the transducer be scanned across the eye multiple times in order to generate a reasonable amount of radiation force across the entire volume of the eye. In an *in-vivo* setting this would be disadvantageous as it increased the overall treatment time by a factor of 3. A brief follow up study (n = 3) was conducted using an Acuson Sequoia system (described in Chapter 1) which has proven effective for delivering ARF.[24] Briefly, the ARF was achieved using a 7 MHz pulse at 28 kPa with a PRF of 25 kHz.

These preliminary results indicated that even with an effective ARF pulse, no movement of

MCAs toward the posterior of the eyes was achieved. Possible reasons for the failure of ARF

to move contrast medium is discussed below.

Effects contributing to MCA distribution

The majority of imaged eyes contained two distinct regions where MCAs accumulated,

around the lens and in the rear of the eye. Significantly less contrast medium was seen along

the sides of the globes. The geometry of the SCS may be responsible for this bimodal

distribution, or other factors may be at work. Because MCAs are gas filled, they experience a

buoyancy force; therefore the orientation of the eyes to gravity will play a role in MCA

distribution. All eyes for this study were imaged with the lens facing up. For *in-vivo* applications

this orientation may be difficult or impossible to achieve depending on the species under

investigation. It therefore is important to ascertain the effect of eye orientation on the

distribution of MCAs. From the ultrasound images collected, there was no evidence that the ARF

parameters used in this study were effective at altering the distribution of contrast agents

within the eye. It is possible that between the application of ARF and the subsequent imaging,

MCA buoyancy could have undone the effect of ARF. This however seems unlikely as the drag

forces on small MCAs mean that their rise through a liquid column is relatively slow.

An additional factor affecting MCA distribution is external and internal pressure. Eyes

for this study were fully separated from the rest of the head anatomy and freely seated in

ultrasound gel, and care was taken to avoid applying pressure to the globes with the transducer.

The effect of pressure, both from the transducer and from the eye socket, may alter the shape

and distension of the SCS. Internal pressure from expansion of the SCS itself was evident, as

after injection of MCAs, small amounts were clearly visible exiting from the injection site. The

spherical nature of the SCS is likely to diminish the effectiveness of ARF application. The

curvature of the eye means that only in a small region is all of the energy from ARF parallel to a

direction which a bubble can actual follow. Near the top of the eye, where much of the contrast

agents collects via floatation, most of the energy is normal to the outer layer of the choroid,

rather than tangential to it. As a result, bubbles were likely forced against the choroid instead of

forced to move along it.

Finally, while it seems most likely that the application of ARF had little effect on

distribution of MCAs, it is possible that any effect was hidden due to saturation of the

ultrasound images. As a result, any additional contrast agents entering saturated regions of

the images would not be detectable in images. Adjustment of gain and dynamic

compression of the images should be adjusted to prevent saturation from occurring.

Effects contributing to drug distribution

The DiI concentrations as measured by spectrofluorometry also showed no effect in

increasing concentration toward the rear of the eye. However, concentrations of DiI in the

retina and vitreous did increase with application of ARF. To reach these tissues, DiI needs to

pass through the choroid. It was beyond the scope of this study to ascertain if this occurred

while still incorporated into a microbubble shell or, more likely, if it occurred after microbubble

destruction. Cellular permeability and sonoporation could be increased in ARF treated eyes, due

to the greater amount of ultrasound energy applied. This is a possible explanation for the

increase in DiI concentration in the retina and vitreous for the treated eyes.

The dye used in this study, DiI, is a fluorescently labeled lipid. Different marker

molecules or actual drug molecules will have different diffusion properties and would likely

distribute throughout the eye tissues in different ways. SCS treatments in an *in vivo* eye face the

additional diffusion barrier of the choroidal circulation. In order to cross from the SCS into the

retina, drugs need to avoid being washed out or diluted by this barrier. Testing of *ex vivo* eyes

which are artificially perfused with saline or a blood substitute will help elucidate the effect on

therapeutic dose delivered to the retina.

Other injection techniques

Research by Park et al.[11] has shown that microbubbles may be used to disrupt the retina

blood barrier. This may prove a more effective method for delivering drugs to the retina than

ocular injection. A comparison of the effectiveness of this technique with ocular injection is

warranted. However, this would require *in-vivo* experiments since effects of blood flow and

tissue perfusion would have significant effects on the outcome.

Clearance of MCAs from the SCS

In the blood stream, MCAs are cleared by diffusion of gas from the core into the

bloodstream,[62] and by immune responses;[63] however, the clearance rates and mechanisms have

not yet been studied in the SCS. In the present study, MCAs were fragmented using destructive

ultrasound pulses, but it is not guaranteed that all MCAs could be fragmented during an *in vivo*

study.

CHAPTER 3.

Controllable microfluidic synthesis of multiphase drug-carrying lipospheres for site-targeted therapy‡

Introduction

Recent advances in molecular biology and genetic research have made possible the creation of more powerful and effective cancer therapeutics, bringing about the realization of the century-old concept of ''magic bullets'' that can carry therapeutic drugs to target sites with high specificity.[64] Efficient carrier-based systems are of increasing importance because of the growing number of active pharmaceutical ingredients (API) with low bioavailability.[65] One of the biggest limitations with current cancer therapy with chemotherapeutics has been the systemic toxicity involved, especially with the intravenous or oral administration route. A lack of selectivity to tumor tissues impedes the therapeutic potential of anticancer drugs.[66] Advances in chemotherapeutics include encapsulating these cytotoxic drugs in a liposome to minimize systemic effects.[67,68] Liposomes consist of single or multiple concentric lipid layers (lamellae) that encapsulate an inner aqueous core. Hydrophilic drugs can be carried in the aqueous compartment of a liposome, and hydrophobic drugs can be incorporated in the lipid bilayer. Polymers such as polyethylene glycol (PEG) can be attached to the surface for stabilization and increase liposome residence time in the blood

_____

circulation, and particular ligands such as antibodies or peptides can be attached to increase

specificity for target sites.[69] By tailoring the size, material characteristics, or shell

components of the liposome, researchers have been able to achieve some specificity of

where these vehicles accumulate, preferentially in tumors.[70] Several major FDA-approved

cytotoxic liposomal formulations (e.g. DaunoXome®, DepoCyt®, Doxil®, and Myocet®)

have been in the market since the 1990s. Liposome-based products however suffer from

relatively nonspecific biodistribution after injection. Accumulation of liposomes by size

selection or molecular targeting is a slow process.[71] It is desirable to minimize nonspecific

drug carrier accumulation because of the toxicity involved with most chemotherapeutic

agents.

Although an API can passively diffuse into a liposome, encapsulation yields are often

small, especially when the API possesses some degree of membrane permeability. Active

encapsulation methods involving, for example, a gradient in pH or chemical potential[72] have

improved yields, but release of the API in a controlled manner is often a challenge. Release

mechanisms range from passive means such as liposome disintegration or diffusion-driven

leakage to more active release methods triggered by external or environmental stimuli such

as a change in pH, temperature, or enzymatic degradation.[73–75] Regardless of a passive or

active mechanism, an unpredictable release profile will lead to a lack of control in drug

release.

One method that has shown initial promise for controlling particle localization and

disruption is ultrasound.[14] Standard liposomes are not acoustically active because their

density and compressibility are similar to the surrounding blood. Microbubble carriers are

uniquely suited for ultrasound enhanced local drug delivery because they can be selectively

concentrated and disrupted at the region of the acoustic focus.[60] Additionally, the rapid

mechanical oscillation of microbubbles in an acoustic field has been shown to enhance the delivery of compounds across cell membranes[76] as well as result in local increases in vascular permeability.[77,78] These stabilized gas microbubbles are used in the clinic today as ultrasound contrast agents to enhance the reflectivity of perfused tissues in applications spanning cardiology[79] and radiology.[80] Although molecularly targeted agents have not yet been applied clinically, preliminary studies have demonstrated application in vascular inflammation and angiogenesis, where researchers have shown the effectiveness of targeted lipid microbubbles as a diagnostic tool in detecting tumors and metastatic spread by assessing the degree of new blood vessel growth.[81–83] However, the thin microbubble shell and gas core each have limited drug-carrying capacity. Researchers have recently created a new drug delivery vehicle by mounting the liposomes on microbubble shells.[15] This new vehicle possesses the drug payload capacity of liposomes yet can still be concentrated with ultrasound radiation force and disrupted with the higher energy acoustic pulses.

The utilization of multilayer gas lipospheres capable of delivering bioactive substances at high concentrations is an interesting prospect for the development of cancer treatments. [26] As shown in Figure 13, such lipospheres possess a layer with drug-carrying capacity (such as oil) and a gas core with significantly different density and compressibility than the surrounding liquid media, providing contrast for ultrasound imaging. These vehicles can be steered, concentrated, and disrupted with ultrasound, both *in-vitro* and in *ex-vivo* microvasculature.[84] Gas lipospheres however are challenging to produce in a controlled manner because of current manufacturing processes. Conventional production techniques involve the use of mechanical agitation[85] or sonication[86], both of which create a highly polydisperse population. Thus, the drug dosages within each vehicle are also not consistent, and microscopy often shows a percentage of vehicles without any gas at all, leaving them

acoustically inactive. The size distribution of the vehicle is extremely important because parameters such as the destruction threshold, amount of radiation force experienced, resonant frequency (important for imaging), and biodistribution are significantly affected by the vehicle diameter.[60,87,88]
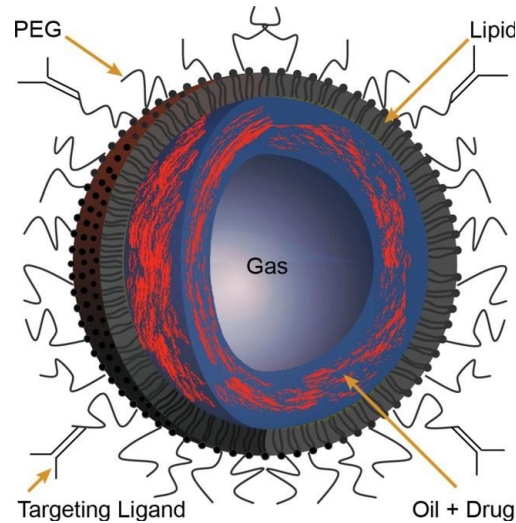

Figure 12. Schematic of a multilayer gas liposphere with targeting capability, carrying therapeutics in the lipid-oil complex.

To control particle synthesis and drug encapsulation, our manufacturing strategy utilizes microfluidics technology. The versatility in function and application of the microfluidic platform has provided unique solutions to healthcare problems within a span of just a few years.[89–94] Microfluidics is one of the few technologies that is able to produce fluid emulsions with high precision.[95] Microfluidic techniques have already shown to be powerful technologies for the generation of highly controlled droplet dispersions[96–99] and microbubbles.[100-103] An additional major advantage of microfluidics is that the potential also exists for manipulating the chemistry and material characteristics of droplets or particles

within the devices so that different functional properties are added for a given application. Using microfluidic flow-focusing, we recently demonstrated the production of lipid-based microbubbles with a much narrower size distribution than commercially available for use as ultrasound contrast imaging agents.[103] A monodisperse microbubble population leads to a more consistent echo response and the potential for higher sensitivity in molecular imaging.

In this work, we report the ability to generate functionalized multilayer gas lipospheres with precisely controlled size and drug carrying capacity. Previous works in the literature have demonstrated the application of multilayer lipospheres as drug delivery agents, but those vehicles were produced with techniques that resulted in size and loading inconsistency. This is the first such article that describes a system for providing a high level of manufacturing control in the production of these complex (three-phase) biocompatible particles. Our microfluidic device in Figure 14 combines two hydrodynamic flow-focusing regions together and features expanding nozzle geometry to generate monodisperse gasfilled lipospheres. The same design may be used to generate single or multilayer gas lipospheres.
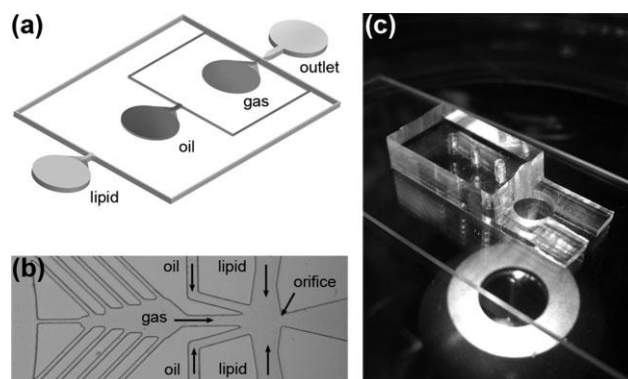
Figure 13. Geometry of device for gas liposphere production. (a) Schematic view of the microfluidic flow-focusing device. All channels have a rectangular cross section and a height of 25 lm. (b) Main functional area with a 25 lm orifice and filtering channels. The arrows indicate direction of flow. (c) 3D view of assembled PDMS device on an inverted microscope.

Materials and methods

Photolithography and fabrication

Fabrication of devices followed standard soft lithography techniques.[104] Briefly, fluidic channel geometries were designed in Illustrator (Adobe) and printed at 20,000 dpi onto transparency masks by CAD/Art Services (Bandon, OR). In a class 10,000 clean room, a 3 in. silicon wafer was first oxidized in oxygen plasma for 10 min at 200 W and 100 mTorr and then spin-coated at 2,000 rpm with a UVcurable epoxy (SU-8-25, MicroChem) to form a 25 μm high layer. Exposure to UV light through the photomask containing the channel pattern crosslinks the exposed areas of SU-8, which then remain on the wafer after development.

The wafer was used to cast a replica in the silicone elastomer polydimethylsiloxane (PDMS) (Sylgard 184, Dow Corning), consisting of a 10:1 prepolymer and curing agent ratio. PDMS as a stamp material has favorable properties such as optical transparency and wide solvent compatibility. The prepared mixture of PDMS was degassed under vacuum, poured

onto the wafer with template, and cured for at least 4 h at 65°C in a temperature-controlled

dry oven. The cured PDMS was peeled from the wafer in a laminar flow hood. Inlets and

outlets were punched with a blunt 18 G needle, and the stamp was bonded to clean soda

lime glass (Corning) after 90 s of air plasma (200 mTorr, 200 W) treatment with an expanded

air plasma cleaner (Harrick Scientific, NY). To preserve the hydrophilicity of the PDMS after

plasma preparation, channels were immediately filled with DI water.

Lipid materials and preparation

The lipid flow stream contains an aqueous glycerol/propylene glycol (GPW) mixture

from Sigma (St Louis, MO) with the stabilizing lipids DSPC (1,2-distearoyl-sn-glycero-3-

phosphocholine, Avanti Polar Lipids) and polyethylene glycol (PEG) lipid conjugate DSPE-

PEG2000-Biotin (1,2- distearoyl-sn-glycero-3-phosphoethanolamine-N-

(biotinyl(polyethylene glycol)2000), Avanti Polar Lipids) at a concentration of 0.5 mg mL^{-1}

DSPC. These lipid shell components are similar to those commonly used for formulation of

lipidencapsulated ultrasound contrast agents.[105]

First, DSPC and DSPE-PEG2000-Biotin were combined at a 9:1 molar ratio and

dissolved in chloroform (CHCl3, Sigma) to create a homogenous mixture. The solvent was

evaporated with a nitrogen stream, exposed to vacuum, and allowed to dry. DiI-C18 (1,10-

dilinoleyl-3,3,30,30-tetramethylindocarbocyanine perchlorate, Molecular Probes) was then

added at 1 mol % for fluorescence microscopy studies of the outer lipid shell layer. Ultra-

pure water was added to the vial containing the dry lipid mixture, sonicated at room

temperature for 20 min, and combined with glycerol/propylene glycol to form a 10% GPW

mixture. The solution was again sonicated during preparation and immediately before using

at 37°C to prevent unwanted liposome formation. To ensure air saturation, the lipid solution was stirred overnight in a 1 atm air environment.

System assembly

The PDMS microfluidic device was placed on an inverted fluorescence microscope (TE2000, Nikon) before external fluidic connections are made. Nitrogen (N_2, Airgas) for multilayer gas lipospheres or octofluorocyclobutane (C4F8, Specialty Chemical Products) for single-layer gas lipospheres were supplied from pressurized tanks via clear TygonVR tubing and delivered into the gas inlet of the microfluidic chamber using a homemade micro flow meter. The continuous liquid (lipid and oil) phase mixtures in 3 cc Becton-Dickinson syringes were pumped into the microfluidic device via 23 G hypodermic tubing at constant flow rates using two digitally controlled syringe pumps (Pico Plus, Harvard Apparatus). A high-speed camera (Fastcam PCI-10K, Photron) was used to capture monochrome still images and record movies. A file viewer (PFV, Photron) and image analysis program (ImageJ, NIH) were used for data processing and measurements. The polydispersity index $\sigma = \delta / d_{avg} \times 100\%$ was calculated from the average vehicle size d_{avg} and standard deviation δ, determined by measuring the sizes of at least 100 gas lipospheres from recorded images.

Cell culture

Minimum essential medium (MEM), sodium pyruvate, sodium bicarbonate, trypsin/EDTA, gentamicin, and fetal bovine serum (FBS) were obtained from Invitrogen (Carlsbad, CA). Phosphate buffered saline (PBS) and collagen type IV were obtained from Sigma (St Louis, MO). The human metastatic breast cancer cell line MDA-MB-231 was donated and originally purchased from American Type Culture Collection (Manassas, VA).

The cells were cultured in MEM supplemented with 10% FBS and sodium pyruvate, sodium bicarbonate, gentamicin at 37°C in a 5% CO2 incubator. Cells were grown on cover slips coated with collagen type IV (100 μg mL^{-1}) to provide an adherent surface for cells. Labeling of the cytoskeleton was performed on live adherent cells in culture plates using TubulinTracker Green reagent (T34075) from Invitrogen (Carlsbad, CA). Mitochondria were stained with MitoTracker Deep Red 633 (M-22426) from Invitrogen (Carlsbad, CA), and the nucleus was stained blue with Hoechst 33342 (H1399) from Invitrogen (Carlsbad, CA). Labeling occurred predominately on the exposed surface.

Biotin (EZ-Link Sulfo-NHS-LC-Biotin, Pierce) binds with high affinity to avidin and was used for labeling of cell surface proteins. MDA-MB-231 cells adherent to glass cover slips were washed with ice-cold PBS three times to avoid amine-containing components competing and quenching the reaction to cell surface proteins. Cells were suspended at a concentration of ~25 ×10^6 cells mL^{-1} in PBS (pH 8.0) and then incubated in 1.0 mg mL^{-1} biotin/PBS solution (results in ~2 mM biotin reagent) for 30 min at room temperature before rinsing with a PBS and 100 mM glycine solution.

Imaging and binding

Gas liposheres in the form of foam were collected using a glass pipette from the outlet reservoir for imaging of the stained lipid membranes. Aliquots were transferred onto glass slides and secured with plastic cover slips to reduce fluid flow and contain the liposheres. The sample was positioned on the microscope stage, and detection of fluorescence occurred at λ = 569 nm due to DiI labeling.

For visualization of the inner oil layer, triacetin oil (Glyceryl triacetate, Sigma), capable of carrying bioactive substances, was premixed with Oil Blue N dye from Sigma (St

Louis, MO) at a concentration of 0.01 mg mL^{-1}. The viscosity of triacetin (28.0 cP) is

considerably less compared with other oils, making it ideal for use at the desired liquid flow

rate regimes of 0.25–0.50 µL s^{-1} in the microchannels. Doxorubicin (Dox) from Sigma (St

Louis, MO) was used as the model antitumor drug because of the intrinsic fluorescence

properties of the molecule. Dox was mixed with triacetin at a concentration of 1 mmol L^{-1}.

Drug concentration of Dox (ex λ = 470 nm; em λ = 585 nm) within the oil layer was visualized

by fluorescence microscopy with rhodamine optics.

For gas liposphere-cell binding studies, 10 µL of Avidin (ImmunoPure Avidin, Pierce)

was added to 500µLof biotinylated vehicles. After 5 min, the vehicle solution was washed

with DI water several times. The mixture was collected with a glass pipette and applied

directly to the adherent cells on collagen type IV-coated cover slips and imaged with an

Olympus BX-41 microscope and CytoViva imaging system consisting of a high-resolution

illuminator, dual mode fluorescence module, and Exfo fluorescence light source. Gentle

movement of the cover slips was sufficient to achieve some degree of binding between the

floating gas lipospheres and the adherent cells at the bottom.

Acoustic response

The acoustic response of 15-lm multilayer gas lipospheres was measured as they

were pumped at a low concentration through a 200 micron acoustically-translucent tube

suspended in a water bath on the inverted microscope. Vehicles were excited with a 1 cycle,

2.25 MHz acoustic pulse at ~200 kPa using a spherically focused ultrasound transducer

(V305, Panametrics), energized with an arbitrary waveform generator (AWG2021, Tektronix)

and amplifier (3200L, ENI). The transducer was positioned in the water bath, and the

acoustic focus was aligned with the translucent tube. Echo signatures for each gas

liposphere were received using a second 2.25 MHz transducer, amplified by 40 dB (BR640, Ritec) and then recorded using a 14-bit, 100 MHz digitizer (PDA14, Signatec) through a LabView (National Instruments Corporation, Austin, TX) interface. Offline processing in Matlab (The Mathworks, Natick, MA) was used to calculate the average correlation between echoes. The size distribution of the polydisperse microbubbles used as a control was similar to the size distribution of Definity® (Lantheus Medical Imaging, North Billerica, MA), an ultrasound contrast agent approved by the US Food and Drug Administration (FDA).

Results and discussion

Device parameters

Liposphere size and production rate are highly prone to downstream pressure conditions in microfluidic channels. Thus, channel geometry and the liquid and gas flow rates are important parameters for stable production and precise control of the liposphere sizes. Combining two hydrodynamic flow-focusing geometries together into a single region proved less sensitive to gas pressure than in double flowfocusing geometry where the two flow-focusing regions are separated by an arbitrary distance. This was critical to the stable formation of smaller sized multilayer gas lipospheres. The gas inlet distance from the orifice region was minimized to reduce gas diffusion and reduction in the widths of the liquid and gas inlet channels to 30 and 20 μm, respectively, enabled the use of lower liquid flow rates and gas delivery pressures to generate micron-sized lipospheres. To reduce bubble contact, the outlet reservoir immediately followed the expansion chamber. The liposphere volume V depends on the ratio of the gas pressure P and overall liquid flow rate Q_t, which is a combination of the oil and lipid/water flow rates Q_0 and Q_w. V increases linearly with P for a fixed Q_t. An increase in Q_t results in a decrease in V.

For the production of gas lipospheres, a pressure drop must occur along the longitudinal axis of the device until the tip of the gas stream breaks at the orifice. We found that the most stable production regime occurs when the oil and lipid/ water phase form an interface of equal pressure upstream of the orifice. Because of the large viscosity difference between triacetin oil and water (28.0 cP vs. 1.0 cP), the oil flow rate Q0 was minimized as much as 30-times less in comparison to the lipid/water flow rate Q_w. Channels were also designed to minimize the contact time and angle between the oil and gas flow streams just prior to the orifice. Because PDMS has the characteristics of high-diffusion coefficients to gases such as nitrogen, reducing the distance between the gas inlet and orifice results in a lower P necessary to produce the same V for a fixed Q_t.

Generation and stability

By simple adjustments in flow parameters, differently sized gas lipospheres were produced using the same microfluidic flow-focusing device. The flow condition relationships can be found in Figure 15a. Stable production rates of 6×10^4 multilayer gas lipospheres per minute have been recorded from a single chamber, requiring several hours to achieve an estimated 2×10^7 vehicles necessary for imaging and drug delivery. This relatively slow production rate currently limits our microfluidics system for use as a viable bulk manufacturing process. The PDMS devices are however robust enough for consistent production of gas lipospheres, and runtimes that last more than 6 h have frequently been observed. Multiplexing several flow-focusing circuits together will also lead to higher throughput and time and cost savings. A 10-fold scale-up of microbubble contrast agent production in our lab has been achieved without a significant change in dimensions of the

device. We feel that future device design improvements will likely allow for large-scale production of these vehicles.
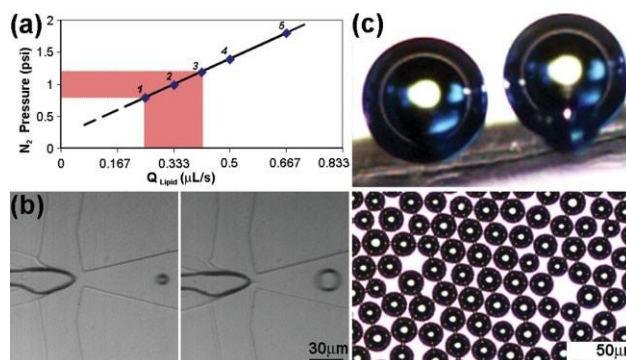

Figure 14. Flow rate vs. size relationships. (a) The optimum flow rate regime (highlighted) to produce <15 lm multilayer liposheres, with five different flow condition points (filled diamonds) that produce mean liposhere sizes of {11, 7, 17, 22, 30 ± 0.2 µm}, respectively. (b) High-speed images showing changes in gas liposhere size upon application of a low lipid/water flow rate of 0.33 µL s^{-1} (left) and a high lipid/water flow rate of 0.5 µL s^{-1} (right). The widths of the liquid, oil, and gas inlet channels are 30 µm, 25 µm, and 20 µm, respectively, and the orifice size is 25 µm. (c) Images showing close-up of two multilayer liposheres clearly showing the inner blue oil layer (top) and monodisperse multilayer gas liposheres visible in brightfield (bottom).

As can be seen in Figure 15b, the smaller sized (7.5 ± 0.2 µm) gas liposheres were produced at a lipid/water flow rate of 0.33 µL s^{-1} and a gas pressure of 1.0 psi, while the larger sized (>20 lm) vehicles were produced at a lipid/water flow rate of 0.5 µL s^{-1} and gas pressure of 1.6 psi and higher. The oil flow rate Q_0 was set at a constant 0.016 µL s^{-1}. We found that the smaller liposheres undergo dissolution to a terminal size where the shell achieves very low-surface tension as they were rising to the top. These liposheres remain stable over the experimental period of 3 h. Increasing the gas and liquid flow rates however decreases the distance between exiting liposheres. These contact interactions cause them to coalesce due to the lower shell resistance in a highflow velocity environment of the microfluidic expansion chamber, destroying the desired monodispersity of the bubble

population. Growth in size was also seen for many of the larger (>20 lm in diameter) vehicles after they reached the outlet reservoir, typical of Ostwald ripening.[106] Because the gas lipospheres rise to the surface producing a highly concentrated layer known as a cream, reducing vehicle size (a function of flow parameters) or increasing the viscosity of the continuous lipid/water phase will delay the rise time and creaming. Varying the percentages of glycerol/propylene glycol will change the viscosity of the solution, and can therefore be used to optimize microbubble stability. With sufficient time, vehicles that reach their terminal size form a fully compressed lipid monolayer shell that has reached a near zero surface tension.[107]

We are currently exploring improved methods of stabilizing these drug delivery vehicles. Possible solutions to improve long-term stability may include adding polaxamers, a different PEG group, or photopolymerizable lipids. However, it may not be necessary to substantially increase shelf life if the vehicles can be manufactured at the point-of-care. Clinical (FDA-approved) lipid contrast agents that are formed via mechanical agitation are injected immediately into the patient, eliminating the need for long-term stability. Testing *in-vivo* will be necessary to determine circulation lifetime, as the blood pressure and dissolved gas concentration may affect stability.

Structure visualization

The outer DSPC lipid shell stabilizes the vehicle and the inner triacetin oil layer can contain dissolved therapeutics. Using a lipid dye, DiI, fluorescence microscopy images of these monodisperse vehicles were taken to confirm the lipid coating on the vehicle surface. The inner dark blue layer confirms the existence of the additional triacetin oil layer. The volume fraction of the oil layer can be adjusted using flow rates for varying the

chemotherapeutic drug concentrations. The gas interior makes the vehicle acoustically active to ultrasound pulses. Low polydispersity values (<5%) demonstrate the advantage of the microfluidic method of manufacture. In contrast, multilayer gas lipospheres capable of carrying consistent drug payloads cannot be reliably made with standard mechanical agitation techniques. Such lipospheres have high-polydispersity values of >50%.[26]

Microfluidic-generated multilayer gas lipospheres are visible in brightfield after being collected on the cover glass, as seen in Figure 16a. A 10 μm gas liposphere contains ~0.5 pL of drug-carrying capacity. Based on an analysis of fluorescence measurements, standard curves of Dox dissolved in triacetin were used to estimate the drug content in the gas lipospheres. Dox is a naturally fluorescent anthracycline antibiotic and anticancer drug. It has been prepared in liposomal formulations as Doxil® and Myocet® to treat kaposi's sarcoma (KS) and metastatic breast cancer. The pattern of Dox fluorescence did not change remarkably in the vehicle suspensions after 1 h of monitoring. As seen in Figure 16b, the sharp boundary is due to the partitioning of Dox preferentially at the boundary of the lipid/oil layer. This is expected as Dox favors the lipid layer, and the drug has not been observed to leach out spontaneously. At the 1 mmol L^{-1} concentration of drug used in this study, the total amount of Dox entrapment is estimated at 15 mg mL^{-1} of packed particles. In a dual-layer vehicle, a large volume fraction of the oil phase can be used and other chemotherapeutic drugs such as Paclitaxel, which exhibits good solubility in triacetin (70 mg mL^{-1}), can be incorporated at high concentrations. At this concentration, ~2.5 mL of suspension would be necessary for an average dose in a human patient. Until now, the ability to accurately control the amount of drug in each vehicle has not been possible.
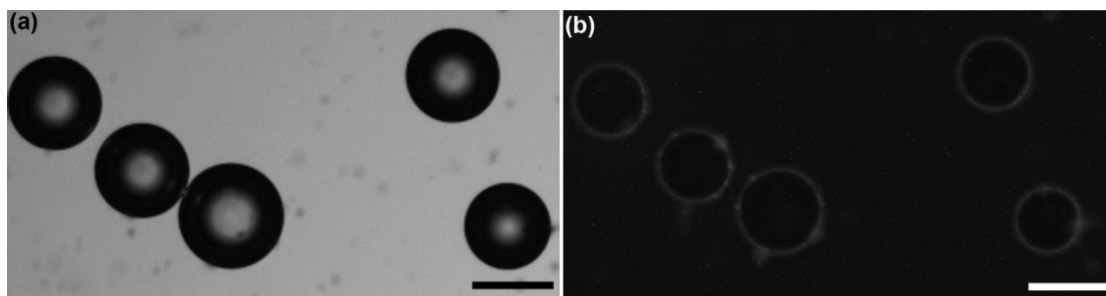
Figure 15. Microscopy images of multilayer gas lipospheres containing Doxorubicin. (a) Brightfield image of lipospheres. Scale bar is 15 lm. (b) Fluorescence image of lipospheres showing Dox fluorescence within the lipid-oil complex. Scale bar is 15 μm.

Cell targeting

To demonstrate the targeted binding of monodisperse gas lipospheres to cancer cells and potential for localized chemotherapeutic drug delivery, we functionalized our vehicles by incorporating biotinylated lipid into the shell. Many current targeted molecular imaging methods involve using the avidin-biotin interaction.[108] The avidin-biotin interaction is the strongest noncovalent interaction between a protein and ligand. Without the conjugation, we have seen that the gas lipospheres will float on the top of the solution and will not adhere to the anchored biotinylated cells at the bottom. On collection of the functionalized gas lipospheres, it was necessary to perform gentle movement of the cover slips to achieve some degree of binding. The live, labeled MDAMB- 231 breast cancer cells remained viable for up to 5 days of culturing under constant perfusion of media, but died in a matter of hours on cover slips from stress due to experimental conditions.
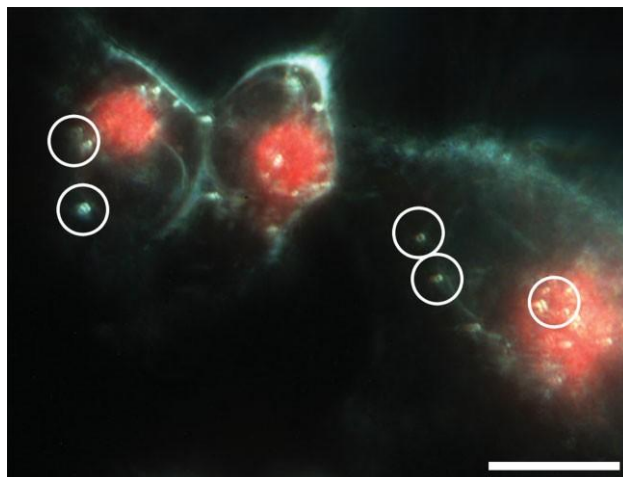
Figure 16. Several monodisperse gas lipospheres capable of carrying drug (circled in white) attached to human metastatic breast cancer cells (MDA-MB-231). The cells are labeled at low-passage density with MitoTracker Red, and the nucleus stained with Hoechst 33342. Scale bar is 100 µm.

As shown in Figure 17, biotinylated gas lipospheres with the avidin linker bound to biotinylated MDA-MB-231 breast cancer cells are visible in fluorescence microscopy. It is possible to have multiple gas lipospheres bound to a single cell, and the binding efficiency depends largely on liposphere size. Gas lipospheres <10 lm in diameter were found to more favorably target the cells than larger vehicles. The vehicles remained bound through cell death, ~1 h into the experiment. Because of the possibility of an immunogenic response with avidin or Streptavidin, we anticipate an alternative conjugation method besides avidin-biotin will be used for future targeted drug delivery to tumor vasculature or other target sites.

Acoustic response

From an m-mode ultrasound image of 12 echoes, as shown in Figure 18a, the acoustic response of 15 µm multilayer gas lipospheres can be determined. Average correlation was measured to be ~0.97, indicating that the echo signatures were nearly

identical. This is in contrast to previous measurements of commercially-available polydisperse contrast agents, which exhibit echo correlations on the order of 0.7. A comparison can be found in Figure 18b. The nearly identical signatures mean that we can optimize ultrasound concentration and drug-release parameters to affect all gas lipospheres similarly. In contrast, for a polydisperse drug delivery vehicle, ultrasound may be able to fragment a 5 µm vehicle but not a 10 µm vehicle due to the different acoustic parameters required to affect vehicles of different size and corresponding different resonant frequencies. Future experiments will study the acoustic parameters required to concentrate the vehicles with ultrasound radiation force and locally release drug payloads at the target site.
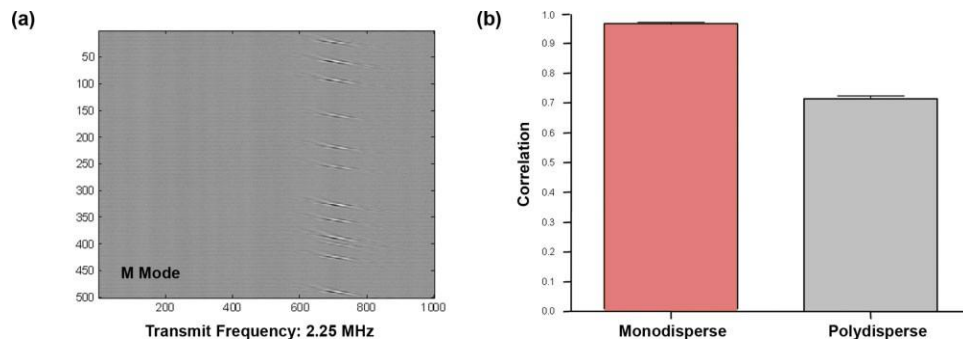

Figure 17. Acoustic response of 15 µm multilayer gas lipospheres. (a) M-mode ultrasound image of 12 gas liposphere echoes, with a mean echo correlation of 0.97. (b) Echoes of individual gas lipospheres were more correlated for a monodisperse population produced with microfluidics compared with a standard polydisperse microbubble population produced with mechanical agitation.

Conclusions

With microfluidics technology, we can produce monodisperse multilayer gas lipospheres in a suitable size range for local injection into tumor sites. Their composition allows them to be both ultrasonically active and able to carry a large and precise drug payload to the target site. Precision engineered multilayer gas lipospheres are much more

57

consistent in their response to ultrasound radiation force. We expect this to directly translate into uniform drug release and improved imaging characteristics compared with polydisperse vehicles.

Vehicles can be further developed by having very specific targeting ligands on the shell surface. As proof-of-concept, we produced vehicles containing biotin groups with avidin linkers on the shell for attachment to biotinylated breast cancer cells, and have demonstrated loading with a model drug Doxorubicin. Conjugating a cyclic-RGD (cyclo[Arg-Gly- Asp]) peptide to the shell to enhance vehicle retention in tumor vasculature that over express the $\alpha_v\beta_3$ integrin is a possibility for targeted delivery. On binding, the narrow size distribution will enable consistent vehicle disruption at the lowest mechanical index (MI) possible.

The controlled production of multilayer microbubble lipospheres using the microfluidic platform provides exciting opportunities for cancer research. We believe similar technology can be applied to generate vehicles that carry hydrophilic drugs as well. The incorporation of a small gas bubble within water or hydrophilic core contained within a secondary shell would make an acoustically-active drug delivery vehicle for hydrophilic molecules. A nice prospect is that when using these vehicles with ultrasound, we can expect to not only deliver and release chemotherapeutic-containing vehicles for therapeutic purposes with site-specificity and low toxicity, but also the acoustic activity of the vehicles will allow imaging of their distribution within the vasculature and estimation of tumor blood perfusion.

Acknowledgments

Chapter 4.

Conclusions and future research

The work presented herein represents a preliminary investigation demonstrating several techniques which could enhance the effectiveness of therapeutic ultrasound and their use in a novel application. MCAs were successfully shown to reach the posterior region of the eye via an injection into the anterior SCS and were characterized for the entire volume of the eye using 3D ultrasound. Additionally, the delivery of a fluorescent dye was enhanced in tissues of interest with the 3D application of ARF, likely because of ultrasound mediated changes in permeability. The production of monodisperse MCAs capable of carrying hydrophobic therapeutic compounds was also demonstrated. While production rates were low, the small volume of the eye represents an ideal platform for initial demonstration of drug delivery using microfluidic production of MCAs.

Several factors of drug delivery in the eye require further study; most importantly, the effect of active perfusion in the *in vivo* environment will have on drug diffusion and distribution. More minor areas of investigation include the effect of buoyancy on MCA distribution altered ocular pressures which may exist for an *in vivo* eye. The use of ARF also requires a specialized transducer or acoustic setting in order to most effectively take advantage of this phenomenon.

References

1. Park MJ, Kim YS, Keserci B, Rhim H, Lim HK. Volumetric MR-guided high-intensity focused ultrasound ablation of uterine fibroids: treatment speed and factors influencing speed. Eur Radiol. 2012 Oct 19.

2. Tandan M, Reddy DN. Extracorporeal shock wave lithotripsy for pancreatic and large common bile duct stones. World J Gastroenterol. 2011 Oct 21;17(39):4365-71

3. Kogan P, Gessner RC, Dayton PA. Microbubbles in Imaging: Applications Beyond Ultrasound. Bubble Sci Eng Technol. 2010 Jun;2(1):3-8.

4. Bracco Diagnostics, Inc. SonoVue Enhanced Ultrasound Versus Unenhanced US for Focal Liver Lesion Characterization. In: ClinicalTrials.gov [Internet]. Bethesda (MD): National Library of Medicine (US). 2008- [cited 2012 Dec 4]. Available from: http://clinicaltrials.gov/ct2/show/NCT00788697 NLM Identifier: NCT00788697

5. Seitz M, Gratzke C, Schlenker B, Buchner A, Karl A, Roosen A, Singer BB, Bastian PJ, Ergün S, Stief CG, Reich O, Tilki D. Contrast-enhanced transrectal ultrasound (CE-TRUS) with cadence-contrast pulse sequence (CPS) technologyfor the identification of prostate cancer. Urol Oncol. 2011 May-Jun;29(3):295-301

6. Chen H, Brayman AA, Kreider W, Bailey MR, Matula TJ. Observations of translation and jetting of ultrasound-activated microbubbles in mesenteric microvessels. Ultrasound Med Biol. 2011 Dec;37(12):2139-48

7. Miller DL, Thomas RM. Ultrasound contrast agents nucleate inertial cavitation in vitro. Ultrasound Med & Biol 1995; 21: 1059-65.

8. Fan Z, Liu H, Mayer M, Deng CX. Spatiotemporally controlled single cell sonoporation. Proc Natl Acad Sci U S A. 2012 Oct 9;109(41):16486-91

9. Caskey CF, Stieger SM, Qin S, Dayton PA, Ferrara KW. Direct observations of ultrasound microbubble contrast agent interaction with the microvessel wall. *The Journal of the Acoustical Society of America* 2007, 122:1191-1200

10. Tung YS, Vlachos F, Feshitan JA, Borden MA, Konofagou EE. The mechanism of interaction between focused ultrasound and microbubbles in blood-brain barrier opening in mice J Acoust Soc Am. 2011 Nov;130(5):3059-67

11. Park EJ, Zhang YZ, Vykhodtseva N, McDannold N. Ultrasound-mediated blood-brain/blood-tumor barrier disruption improves outcomes with trastuzumab in a breast cancer brain metastasis model. J Control Release. 2012 Nov 10;163(3):277-84

12. Chen ZY, Liang K, Qiu RX, Luo LP.Ultrasound- and liposome microbubble-mediated targeted gene transfer to cardiomyocytes in vivo accompanied by polyethylenimine. J Ultrasound Med. 2011 Sep;30(9):1247-58.

13. Phillips LC, Klibanov AL, Wamhoff BR, Hossack JA. Localized ultrasound enhances delivery of rapamycin from microbubbles to prevent smooth muscle proliferation. *J Control Release* 2011, 154:42-49.

14. Lum AF, Borden MA, Dayton PA, Kruse DE, Simon SI, Ferrara KW. Ultrasound radiation force enables targeted deposition of model drug carriers loaded on microbubbles. J Control Release. 2006; 111:128–134.

15. Kheirolomoom A, Dayton PA, Lum AFH, Little E, Paoli EE, Zheng HR, Ferrara KW. Acoustically-active microbubbles conjugated to liposomes: Characterization of a proposed drug delivery vehicle. *Journal of Controlled Release* 2007, 118:275-284.

16. Tlaxca JL, Rychak JJ, Ernst PB, Prasad KM, Shevchenko TI, Pizzaro T, Rivera-Nieves J, Klibanov AL, Lawrence MB. Ultrasound-based molecular imaging and specific gene delivery to mesenteric vasculature by endothelial adhesion molecule targeted microbubbles in a mouse model of Crohn's disease. J Control Release. 2012 Nov 8. doi:pii: S0168-3659(12)00753-5

17. Carson AR, McTiernan CF, Lavery L, Grata M, Leng X, Wang J, Chen X, Villanueva FS.Ultrasound-Targeted Microbubble Destruction to Deliver siRNA Cancer Therapy. Cancer Res. 2012 Dec 1;72(23):6191-9.

18. Streeter JE, Gessner RC, Tsuruta J, Feingold S, Dayton PA. Assessment of molecular imaging of angiogenesis with three-dimensional ultrasonography. Mol Imaging. 2011 Dec;10(6):460-8.

19. Deshpande N, Lutz AM, Ren Y, Foygel K, Tian L, Schneider M, Pai R, Pasricha PJ, Willmann JK. Quantification and monitoring of inflammation in murine inflammatory bowel disease with targeted contrast-enhanced US.Radiology. 2012 Jan;262(1):172-80

20. Phillips LC, Klibanov AL, Wamhoff BR, Hossack JA. Intravascular ultrasound detection and delivery of molecularly targeted microbubbles for gene delivery. IEEE Trans Ultrason Ferroelectr Freq Control. 2012 Jul;59(7):1596-601.

21. Rychak JJ, Klibanov AL, Ley KF, Hossack JA. Enhanced targeting of ultrasound contrast agents using acoustic radiation force. *Ultrasound in Medicine and Biology* 2007, 33:1132-1139.

22. Dayton PA, Klibanov A, Brandenburger G, Ferrara K. Acoustic radiation force in vivo: a mechanism to assist targeting of microbubbles. *Ultrasound Med Biol* 1999, 25:1195-1201.

23. Dayton PA, Morgan KE, Klibanov ALS, Brandenburger G, Nightingale KR, Ferrara KW. A preliminary evaluation of the effects of primary and secondary radiation forces on acoustic contrast agents. *IEEE Transactions on Ultrasonics Ferroelectrics and Frequency Control* 1997, 44:1264-1277.

24. Gessner RC, Streeter JE, Kothadia R, Feingold S, Dayton PA. An in vivo validation of the application of acoustic radiation force to enhance the diagnostic utility of molecular imaging using 3-d ultrasound. *Ultrasound Med Biol* 2012, 38:651-660.

25. Peyman SA, Abou-Saleh RH, McLaughlan JR, Ingram N, Johnson BR, Critchley K, Freear S, Evans JA, Markham AF, Coletta PL, Evans SD.Expanding 3D geometry for enhanced on-chip microbubble production and single step formation of liposomemodified microbubbles. Lab Chip. 2012 Nov 7;12(21):4544-52

26. Unger EC, McCreery TP, Sweitzer RH, Caldwell VE, Wu YQ. Acoustically active liposheres containing paclitaxel - A new therapeutic ultrasound contrast agent. *Investigative Radiology* 1998, 33:886-892.

27. Vu V, Liu Y, Sen S, Xu A, Sweeney G. Delivery of adiponectin gene to skeletal muscle using ultrasound targeted microbubbles improves insulin sensitivity and whole body glucose homeostasis. Am J Physiol Endocrinol Metab. 2012 Nov 6

28. Edelhauser H, Rowe-Rendleman C, Robinson M, et al. Ophthalmic drug delivery systems for the treatment of retinal diseases: basic research to clinical applications. Invest Ophthalmol Vis Sci. 2010; 51:5403–5420.

29. Kim SH, Lutz RJ, Wang NS, Robinson MR. Transport barriers in transscleral drug delivery for retinal diseases. Ophthalmic Res. 2007;39:244 –254.

30. Sampat KM, Garg SJ. Complications of intravitreal injections. Curr Opin Ophthalmol. 2010;21:178 –183.

31. Shima C, Sakaguchi H, Gomi F, et al. Complications in patients after intravitreal injection of bevacizumab. Acta Ophthalmol. 2008;86:372–376.

32. Callanan DG, Jaffe GJ, Martin DF, Pearson   PA, Comstock TL. Treatment of posterior uveitis   with   a fluocinolone acetonide implant: three-year clinical trial results. Arch Ophthalmol. 2008; 126:1191–1201.

33. Einmahl S, Savoldelli   M, D'Hermies   F, Tabatabay C, Gurny R, Behar-Cohen F. Evaluation of a novel biomaterial in the suprachoroidal space of the rabbit eye. Invest Ophthalmol Vis Sci. 2002; 43:1533–1539.

34. Olsen TW, Feng X, Wabner K, et al. Cannulation of the supracho- roidal space: a novel drug delivery methodology to the posterior segment. Am J Ophthalmol. 2006;142:777– 787.

35. Park J, Zhang Y, Vykhodtseva N, Akula JD, McDannold NJ. Targeted and reversible blood- retinal barrier disruption via focused ultrasound and microbubbles.PLoS One. 2012;7(8):e42754.

36. Gessner R, Dayton PA. Advances in molecular imaging with ultrasound. Mol Imaging. 2010 Jun;9(3):117-27.

37. Maurice DM. Drug delivery to the posterior segment from drops. Surv Ophthalmol. 2002;47(suppl 1):S41–S52.

38. Hughes P, Olejnik O, Chang-Lin J, Wilson C. Topical and systemic drug delivery to the posterior segments. Adv Drug Deliv Rev. 2005;57:2010–2032.

39. Lee SS, Hughes PM, Robinson MR. Recent advances in drug delivery systems for treating ocular complications of systemic diseases. Curr Opin Ophthalmol. 2009;20:511–519.

40. Kim H, Csaky KG, Gravlin L, et al. Safety and pharmacokinetics of a preservative-free triamcinolone acetonide formulation for intra- vitreal administration. Retina. 2006;26:523– 530.

41. Kim S, Galban C, Lutz R, et al. Assessment of subconjunctival and intrascleral drug delivery to the posterior segment using dynamic contrast-enhanced magnetic resonance imaging. Invest Ophthalmol Vis Sci. 2007;48:808–814.

42. Krohn J, Bertelsen T. Corrosion casts of the suprachoroidal space and uveoscleral drainage routes in the human eye. Acta Ophthal mol Scand. 1997;75:32–35.

43. Hou J, Tao Y, Jiang Y, Wang K. In vivo and in vitro study of suprachoroidal fibrin glue. Jpn J Ophthalmol. 2009;53:640–647.

44. Olsen TW, Feng X, Wabner K, et al. Pharmacokinetics of pars plana intravitreal injections versus microcannula suprachoroidal injections of bevacizumab in a porcine model. Invest Ophthalmol Vis Sci. 2011;52:4749–4756.

45. Gilger BC, Salmon JH, Wilkie DA, et al. A novel bioerodible deep scleral lamellar cyclosporine implant for uveitis. Invest Ophthal- mol Vis Sci. 2006;47:2596–2605.

46. Patel S, Lin A, Edelhauser HF, Prausnitz M. Suprachoroidal drug delivery to the back of the eye using hollow microneedles. Pharm Res. 2011;28:166–176.

47. Gilger BC, Reeves KA, Salmon JH. Ocular parameters related to drug delivery in the canine and equine eye: aqueous and vitreous humor volume and scleral surface area and thickness. Vet Oph- thalmol. 2005;8:265–269.

48. Shafiee A, McIntire GL, Sidebotham LC, Ward KW. Experimental determination and allometric prediction of vitreous volume, and retina and lens weights in Gottingen minipigs. Vet Ophthalmol. 2008;11:193–196.

49. Bui BV, Edmunds B, Cioffi GA, Fortune B. The gradient of retinal functional changes during acute intraocular pressure elevation. Invest Ophthalmol Vis Sci. 2005;46:202–213.

50. Oz O, Gurelik G, Akyurek N, Cinel L, Hondur A. A short duration transient ischemia induces apoptosis in retinal layers: an experi- mental study in rabbits. Eur J Ophthalmol. 2005;15:233–238.

51. Patel SR, Lin AS, Edelhauser HF, Prausnitz MR. Suprachoroidal drug delivery to the back of the eye using hollow microneedles. Pharm Res. 2011;28:166 –176.

52. Mittl RN. Perfluorocarbon gases in the suprachoroidal space of rabbit eyes. Graefes Arch Clin Exp Ophthalmol. 1990;228:589–593.

53. Mittl RN, Tiwari R. Suprachoroidal injection of sodium hyaluronate as an 'internal' buckling procedure. Ophthalmic Res. 1987;19: 255–260.

54. Rychak JJ, Graba J, Cheung AM, et al. Microultrasound molecular imaging of vascular endothelial growth factor receptor 2 in a mouse model of tumor angiogenesis. Mol Imaging. 2007;6:289–296.

55. Klibanov AL. Microbubble contrast agents: targeted ultrasound imaging and ultrasound-assisted drug-delivery applications. Invest Radiol. 2006;41:354–362.

56. Burke CW, Price RJ. Contrast ultrasound targeted treatment of gliomas in mice via drug-bearing nanoparticle delivery and micro- vascular ablation. J Vis Exp. 2010;46: pii: 2145. doi: 10.3791/2145.

57. Uesugi Y, Kawata H, Jo J, Saito Y, Tabata Y. An ultrasound- responsive nano delivery system of tissue-type plasminogen acti- vator for thrombolytic therapy. J Control Release. 2010;147:269–277.

58. Hynynen K. Focused ultrasound for blood-brain disruption and delivery of therapeutic molecules into the brain. Expert Opin Drug Deliv. 2007;4:27–35.

59. Feingold S, Gessner R, Guracar IM, Dayton PA. Quantitative volu- metric perfusion mapping of the microvasculature using contrast ultrasound. Invest Radiol. 2010;45:669 –674.

60. Dayton PA, Allen JS, Ferrara KW. The magnitude of radiation force on ultrasound contrast agents. J Acoust Soc Am. 2002; 112(5 Part 1):2183–2192

61. Zhao S, Borden M, Bloch SH, Kruse D, Ferrara KW, Dayton PA. Radiation-force assisted targeting facilitates ultrasonic molecular imaging. Mol Imaging. 2004 Jul;3(3):135-48.

62. Mullin L, Gessner R, Kwan J, Kaya M, Borden MA, Dayton PA. Effect of Anesthesia Carrier Gas on In-Vivo Circulation Times of Ultrasound Microbubble Contrast Agents in RatsContrast Media Mol Imaging. Contrast Media Mol Imaging. 2011 May-Jun; 6(3): 126–131

63. Borden MA, Sarantos MR, Stieger SM, Simon SI, Ferrara KW, Dayton PA.Ultrasound radiation force modulates ligand availability on targeted contrast agents. Mol Imaging. 2006 Jul;5(3):139-47

64. Strebhardt K, Ullrich A. Paul Ehrlic h's magic bullet concept: 100 years of progress. Nat Rev Cancer. 2008;8:473–480.

65. Allen TM, Cullis PR. Drug delivery systems: entering the mainstream. Science. 2004;303:1818–1822.

66. Jain RK. Delivery of molecular and cellular medicine to solid tumors. Adv Drug Deliv Rev. 2001;46:149–168.

67. Rapoport N, Pitt WG, Sun H, Nelson JL. Drug delivery in polymeric micelles: from in vitro to in vivo. J Control Release. 2003;91:85–95.

68. Torchilin VP. Recent advances with liposomes as pharmaceutical carriers. Nat Rev Drug Discov. 2005;4:145–160.

69. Immordino ML, Dosio F, Cattel L. Stealth liposomes: review of the basic science, rationale, and clinical applications, existing and potential. Int J Nanomed. 2006;1;297–315.

70. Maeda H. The enhanced permeability and retention (EPR) effect in tumor vasculature: the key role of tumor-selective macromolecular drug targeting. Adv Enzyme Regul. 2001;41:189–207.

71. Gabizon AA, Shmeeda H, Zalipsky S. Pros and cons of the liposome platform in cancer drug targeting. J Liposome Res. 2006;16:175–183.

72. Mayer LD, Reamer J, Bally MB. Intravenous pretreatment with empty pH gradient liposomes alters the pharmacokinetics and toxicity of doxorubicin through in vivo active drug encapsulation. J Pharm Sci. 1999;88:96–102.

73. Ponce AM, Vujaskovic Z, Yuan F, Needham D, Dewhirst MW. Hyperthermia mediated liposomal drug delivery. Int J Hyperthermia. 2006;22:205–213.

74. Gerasimov OV, Boomer JA, Qualls MM, Thompson DH. Cytosolic drug delivery using pH- and light-sensitive liposomes. Adv Drug Deliv Rev. 1999;38:317–338.

75. Thompson DH, Gerasimov OV, Wheeler JJ, Rui Y, Anderson VC. Triggerable plasmalogen liposomes: improvement of system efficiency. Biochim Biophys Acta. 1996;1279:25–34.

76. Postema M, Gilja OH. Ultrasound-directed drug delivery. Curr Pharm Biotechnol. 2007;8:355–361.

77. Stieger SM, Caskey CF, Adamson RH, Qin SP, Curry FRE, Wisner ER, Ferrara KW. Enhancement of vascular permeability with low-frequency contrast-enhanced ultrasound in the chorioallantoic membrane model. Radiology. 2007;243:112–121.

78. Sheikov N, McDannold N, Sharma S, Hynynen K. Effect of focused ultrasound applied with an ultrasound contrast agent on the tight junctional integrity of the brain microvascular endothelium. Ultrasound Med Biol. 2008;34:1093–1104.

79. Wei K, Kaul S. Recent advances in myocardial contrast echocardiography. Curr Opin Cardiol. 1997;12:539–546.

80. Forsberg F, Liu JB, Merton DA, Rawool NM, Goldberg BB. Parenchymal enhancement and tumor visualization using a new sonographic contrast agent. J Ultrasound Med. 1995:14:949– 957.

81. Ellegala DB, Leong-Poi H, Carpenter JE, Klibanov AL, Kaul S, Shaffrey ME, Sklenar J, Lindner JR. Imaging tumor angiogenesis with contrast ultrasound and microbubbles targeted to alpha(v)beta3. Circulation. 2003;108:336–341.

82. Villanueva FS, Wagner WR. Ultrasound molecular imaging of cardiovascular disease. Nat Clin Pract Cardiovasc Med. 2008; 5,S26–S32.

83. Dayton PA, Rychak JJ. Molecular ultrasound imaging using microbubble contrast agents. Front Biosci. 2007;12,5124–5142.

84. Shortencarier MJ, Dayton PA, Bloch SH, Schumann PA, Matsunaga TO, Ferrara KW. A method for radiation-force localized drug delivery using gas-filled liposuheres. IEEE Trans Ultrason Ferroelectr Freq Control. 2004;51:822–831.

85. Tartis MS, McCallan J, Lum AF, LaBell R, Stieger SM, Matsunaga TO, Ferrara KW. Therapeutic effects of paclitaxel-containing ultrasound contrast agents. Ultrasound Med Biol. 2006; 32:1771–1780.

86. Fang JY, Hung CF, Liao MH, Chien CC. A study of the formulation design of acoustically active liposuheres as carriers for drug delivery. Eur J Pharm Biopharm. 2007;67:67–75.

87. Chomas JE, Dayton P, May D, Ferrara K. Threshold of fragmentation for ultrasonic contrast agents. J Biomed Opt. 2001;6: 141–150.

88. Talu E, Hettiarachchi K, Zhao S, Powell RL, Lee AP, LongoML, Dayton PA. Tailoring the size distribution of ultrasound contrast agents: possible method for improving sensitivity in molecular imaging. Mol Imaging. 2007;6:384–392.

89. Chan EM, Alivisatos AP, Mathies RA. High-temperature microfluidic synthesis of CdSe nanocrystals in nanoliter droplets. J Am Chem Soc. 2005;127:13854–13861.

90. Hung LH, Choi KM, Tseng WY, Tan YC, Shea KJ, Lee AP. Alternating droplet generation and controlled dynamic droplet fusion in microfluidic device for CdS nanoparticle synthesis. Lab Chip. 2006;6:174–178.

91. Ramsey JM, Jacobson SC, Knapp MR. Microfabricated chemical measurement systems. Nat Med. 1995;1:1093–1096.

92. Tan YC, Fisher JS, Lee AI, Cristini V, Lee AP. Design of microfluidic channel geometries for the control of droplet volume, chemical concentration, and sorting. Lab Chip. 2004;4: 292–298.

93. Whitesides GM. The origins and the future of microfluidics. Nature. 2006;442:368–373.

94. Zheng B, Roach LS, Ismagilov RF. Screening of protein crystallization conditions on a microfluidic chip using nanoliter-size droplets. J Am Chem Soc. 2003;125:11170–11171.

95. The SY, Lin R, Hung LH, Lee AP. Droplet microfluidics. Lab Chip. 2008;8:198–220.

96. Anna SL, Bontoux N, Stone HA. Formation of dispersions using flow focusing in microchannels. Appl Phys Lett. 2003;82:364– 366.

97. Nisisako T, Torii T, Higuchi T. Droplet formation in a microchannel network. Lab Chip. 2002;2:24–26.

98. Thorsen T, Roberts RW, Arnold FH, Quake SR. Dynamic pattern formation in a vesicle-generating microfluidic device. Phys Rev Lett. 2001;86:4163–4166.

99. Xu Q, Nakajima M. The generation of highly monodisperse droplets through the breakup of hydrodynamically focused microthread in a microfluidic device. Appl Phys Lett. 2004;85: 3726–3728.

100. Ganan-Calvo AM, Gordillo JM. Perfectly monodisperse microbubbling by capillary flow focusing. Phys Rev Lett. 2001; 87(Part 1)274501.

101. Garstecki P, Gitlin I, DiLuzio W, Whitesides GM, Kumacheva E, Stone HA. Formation of monodisperse bubbles in a microfluidic flow-focusing device. Appl Phys Lett. 2004;85:2649–2651.

102. Gordillo JM, Cheng Z, Ganan-Calvo AM, Ma´rquez M, Weitz DA. A new device for the generation of microbubbles. PhysFluids. 2004;16:2828–2834.

103. Hettiarachchi K, Talu E, Longo ML, Dayton PA, Lee AP. On chip generation of microbubbles as a practical technology formanufacturing contrast agents for ultrasonic imaging. Lab Chip. 2007;7:463–468.

104. Xia YN, Whitesides GM. Soft lithography. Angew Chem Int Ed. 1998,37:551–575.

105. Klibanov AL, Rychak JJ, Yang WC, Alikhani S, Li B, Acton S, Lindner JR, Ley K, Kaul S. Targeted ultrasound contrast agent for molecular imaging of inflammation in high-shear flow. Contrast Media Mol Imaging. 2006;1:259–266.

106. Talu E, Hettiarachchi K, Powell RL, Lee AP, Dayton PA, Longo ML. Maintaining monodispersity in a microbubble population formed by flow-focusing. Langmuir. 2008;24:1745–1749.

107. Borden MA, Pu G, Runner GJ, Longo ML. Surface phase behavior and microstructure of lipid/PEG-emulsifier monolayercoated microbubbles. Colloid Surf B Biointerfaces. 2004;35: 209–223.

108. Lanza GM, Wallace KD, Scott MJ, Cacheris WP, Abendschein DR, Christy DH, Sharkey AM, Miller JG, Gaffney PJ, Wickline SA. A novel site-targeted ultrasonic contrast agent with broad